Volume 1 | Number 1 | Jan 2013 | Pages 1–100

Dalton Transactions

An international journal of inorganic chemistry
www.rsc.org/dalton

ROYAL SOCIETY OF CHEMISTRY

www.rsc.org/dalton

The in magnitude somewhat large J values of trinuclear bis(oxamidato) versus bis(oxamato) type complexes are explained by an interplay between different spin density distribution of their related mononuclear precursors.

$J_{12} = J_{13} = -89 \text{ cm}^{-1}$

$J_{12} = J_{13} = -132 \text{ cm}^{-1}$
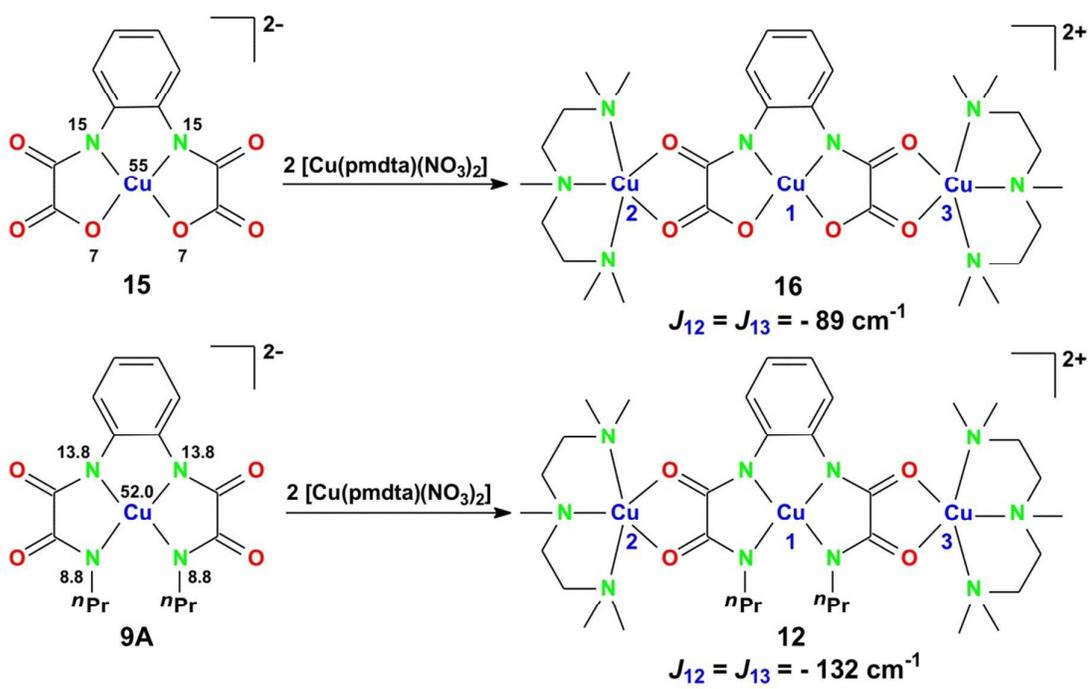
Magnetic superexchange interactions: trinuclear bis(oxamidato) versus bis(oxamato) type complexes†

Mohammad A. Abdulmalic,[a] Azar Aliabadi,[b] Andreas Petr,[b] Yulia Krupskaya,[c] Vladislav Kataev,[b] Bernd Büchner,[b,d] Ruslan Zaripov,[e] Evgeniya Vavilova,[e] Violeta Voronkova,[e] Kev Salikov,[e] Torsten Hahn,[f] Jens Kortus,[f] Francois Eya'ane Meva,[g] Dieter Schaarschmidt[a] and Tobias Rüffer[*a]

[a] Technische Universität Chemnitz, Fakultät für Naturwissenschaften, Strasse der Nationen 62, D-09111 Chemnitz, Germany.
E-mail: tobias.rueffer@chemie.tu-chemnitz.de

[b] Leibniz Institute for Solid State and Materials Research IFW Dresden, D-01171 Dresden, Germany.

[c] Départment de Physique de la Matiére Condensée (DPMC) and Group of Applied Physics (GAP), University of Geneva, 24 Quai Ernest-Ansermet, CH1211 Genéve 4, Switzerland.

[d] Institut für Festkörperphysik, Technische Universität Dresden, D-01062 Dresden, Germany.

[e] Zavoisky Physical Technical Institute, Russian Academy of Sciences, 420029 Kazan, Russia.

[f] Technische Universität Bergakademie Freiberg, Institut für Theoretische Physik, D-09596 Freiberg, Germany.

[g] Department of Pharmaceutical Sciences, Faculty of Medicine and Pharmaceutical Sciences, University of Douala, BP 2701, Cameroon.
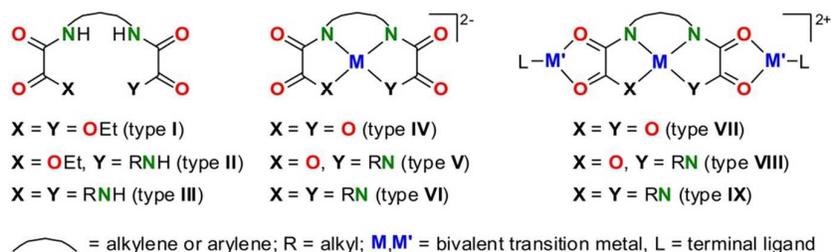
The diethyl ester of $\underline{o}$-phenylenebis(ox$\underline{a}$mic acid) (opbaH$_2$Et$_2$) was treated with excess of RNH$_2$ in MeOH to give the exclusive formation of the respective $\underline{o}$-phenylene$\underline{b}$is(N(R)-$\underline{o}$xamides) (opboH$_4$R$_2$, R = Me **1**, Et **2**, ^{n}Pr **3**) in good yields. Treatment of **1**–**3** with half an equivalent of [Cu$_2$(AcO)$_4$(H$_2$O)$_2$] or one equivalent of [Ni(AcO)$_2$(H$_2$O)$_4$] followed by the addition of four equivalents of [^{n}Bu$_4$N]OH resulted in the formation of mononuclear bis(oxamidato) type complexes [^{n}Bu$_4$N]$_2$[M(opboR$_2$)] (M = Ni, R = Me **4**, Et **5**, ^{n}Pr **6**; M = Cu, R = Me **7**, Et **8**, ^{n}Pr **9**). By addition of two equivalents of [Cu(pmdta)(NO$_3$)$_2$] to MeCN solutions of **7**–**9**, the novel trinuclear complexes [Cu$_3$(opboR$_2$)(L)$_2$](NO$_3$)$_2$ (L = pmdta, R = Me **10**, Et **11**, ^{n}Pr **12**) could be obtained. Compounds **4**–**12** have been characterized by elemental analysis and NMR/IR spectroscopy. Furthermore, the solid state structures of **4**–**10** and **12** have been determined by single-crystal X-ray diffraction studies.

By controlled cocrystallization, diagmagnetically diluted **8** and **9** (1%) in the host lattice of **5** and **6** (99%) (**8@5** and **9@6**), respectively, in form of single crystals have been made available, allowing single crystal ESR studies to extract all components of the g-factor and the tensors of onsite ^{Cu}A and transferred ^{N}A hyperfine (HF) interaction. Out of these studies the spin density distribution of the [Cu(opboEt$_2$)]$^{2-}$ and [Cu(opbo^{n}Pr$_2$)]$^{2-}$ complex fragments of **8** and **9**, respectively, could be determined. Additionally, as a single crystal ENDOR measurement of **8@5** revealed the individual HF tensors of the N donor atoms to be unequal, individual estimates of the spin densities on each N donor atom were made.

The magnetic properties of **10**–**12** were studied by susceptibility measurements versus temperature to give J values varying from –96 cm^{-1} (**10**) over –104 cm^{-1} (**11**) to –132 cm^{-1} (**12**). These three trinuclear Cu^{II}-containing bis(oxamidato) type complexes exhibit J values which are comparable and slightly larger in magnitude as those of related bis(oxamato) type complexes. In a summarizing discussion involving experimentally obtained ESR results (spin density distribution) of **8** and **9**, the geometries of the terminal [Cu(pmdta)]$^{2+}$ fragments of **12** determined by crystallographic studies together with accompanying quantum chemical calculations, an approach is derived to explain these phenomena and to conclude if the spin density distribution of mononuclear bis(oxamato)/bis(oxamidato) type complexes could be a measure of the J couplings of corresponding trinuclear complexes.

Introduction

Over the past three decades the diethyl ester of *N,N'*-alkylene or arylene bis(oxamic acid) (type **I**) have been extensively used for the synthesis of mononuclear bis(oxamato) type **IV** complexes, cf. Scheme 1.[1] The flexidentate properties of the type **IV** complexes paved the way for, e.g., the preparation of their corresponding trinuclear type **VII** complexes which are excellently suited to study magnetic superexchange phenomena.[1,2]

X = Y = OEt (type **I**)   X = Y = O (type **IV**)   X = Y = O (type **VII**)

X = OEt, Y = RNH (type **II**)   X = O, Y = RN (type **V**)   X = O, Y = RN (type **VIII**)

X = Y = RNH (type **III**)   X = Y = RN (type **VI**)   X = Y = RN (type **IX**)

⌒ = alkylene or arylene; R = alkyl; **M,M'** = bivalent transition metal, L = terminal ligand

Scheme 1 Chemical structures of type **I**–**IX** compounds.

On the other hand, the mono-*N*- (type **II**) and di-*N*-substituted (type **III**) type **I** compounds and, thus, their subsequent mononuclear type **V** and **VI** complexes, cf. Scheme 1, have been received less attention.[3-6] Due to this, a limited number of corresponding trinuclear type **VIII** and **IX** complexes, cf. Scheme 1, has been reported so far.[7,8a]

As reported by Kahn,[9] a slight tuning of the ligand skeleton that bridges neighbouring metals, mainly the replacement of the Lewis-basic heteroatoms of the oxamato fragments to less electronegative ones, can induce higher *J* couplings between neighboured, e.g. Cu^{II} ions, as shown for a number of binuclear complexes.

In a recent study, we observed a direct proportion between the spin density distribution of a type **V** complex, namely [^{n}Bu$_4$N]$_2$[Cu(opooMe)] (opooMe = *o*-phenylene(*N'*-methyl oxamidato)(oxamato)) (**13**), and the magnetic superexchange interactions of its corresponding trinuclear type **VIII** complex, namely [Cu$_3$(opooMe)(pmdta)$_2$](NO$_3$)$_2$·3MeCN (**14**).[8a] These results support the assumption, on one hand, that the spin density distribution of mononuclear type **IV** and/or **V** complexes is a measure of the magnitude of *J* values of corresponding trinuclear type **VII**/**VIII** complexes.[8a,10]

On the other hand, the asymmetric type **VIII** complex **14** has been synthesized to verify whether the magnetic superexchange interactions between its oxamato or oxamidato bridged Cu^{II} ions are different or not. However, only one experimentally J value of -130 cm^{-1} was determined, although, for example, from DFT calculations two different J values (-84 cm^{-1}/ -72 cm^{-1} via the oxamidato/oxamato bridging unit) were derived.[8b] This observation agrees with the statement made by Kahn on how to induce higher J couplings.[9] For example, we have already reported on the conversion of $[^nBu_4N]_2[Cu(opba)]$ (**15**) to $[Cu_3(opba)(pmdta)_2(NO_3)](NO_3) \cdot 2MeCN$ (**16**, opba = <u>o</u>-phenylene<u>b</u>is(ox<u>a</u>m<u>a</u>t<u>o</u>)) or of $[^nBu_4N]_2[Cu(obbo)]$ (**17**) to $[Cu_3(obbo)(pmdta)_2(NO_3)](NO_3) \cdot CH_2Cl_2 \cdot H_2O$ (**18**, obbo = <u>o</u>-<u>b</u>enzyl<u>b</u>is(ox<u>a</u>mat<u>o</u>)) with $J = -89$ cm^{-1} and $J = -111$ cm^{-1}, respectively.[11,12] However, additional studies are required to verify this finding.

In order to elaborate the interplay between the spin density distribution of mononuclear type **IV**–**VI** complexes and the magnetic superexchange interactions of their corresponding trinuclear type **VII**–**IX** complexes further, we report here on the synthesis of the mononuclear type **VI** complexes $[^nBu_4N]_2[M(opboR_2)]$ (M = Ni^{II}, R = Me (**4**), Et (**5**), ^nPr (**6**). M = Cu^{II}, R = Me (**7**), Et (**8**), ^nPr (**9**)). Diamagnetically diluted single crystals of **8@5** and **9@6** were prepared to estimate the spin density distributions of **8** and **9** from the HF tensors determined by ESR spectroscopy. Out of **7**–**9** the corresponding type **IX** complexes $[Cu_3(opboR_2)(L)_2](NO_3)_2$ (L = pmdta, R = Me (**10**), Et (**11**), ^nPr (**12**)) were synthesized to determine their magnetic properties. The results obtained thereof are reported here, together with supporting DFT calculations.

Results and discussion

Synthesis

The synthesis of the compounds **1**–**12** is shown in Scheme 2. Thereby, **1**–**3** were synthesized according to a procedure reported by Ruiz *et al.*[3] by the condensation reactions of opbaH$_2$Et$_2$ with excess of alkylamines (**1**: MeNH$_2$, **2**: EtNH$_2$, **3**: ^{n}PrNH$_2$) in MeOH. Compounds **1**–**3** were separated from the reaction mixture by filtration.
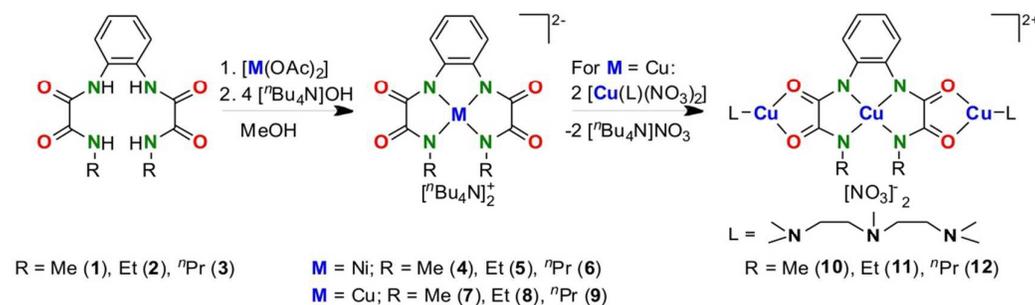
Scheme 2 Synthetic strategy to achieve the mononuclear **4**–**9** and trinuclear **10**–**12** complexes.

For the synthesis of the mononuclear type **VI** complexes **4**–**9**, a hot MeOH solution of [Cu$_2$(OAc)$_4$(H$_2$O)$_2$] or [Ni(OAc)$_2$(H$_2$O)$_4$], respectively, was added to a suspension of either **1**–**3** in MeOH.[13] Then, four equivalents of [^{n}Bu$_4$N]OH were added, causing the complete solution of all suspended material and the reaction mixture was stirred for 15 min at 60 °C. The complexes **4**–**9** were isolated after appropriate workup as yellow and red powders.[13]

The trinuclear type **IX** complexes **10**–**12** were synthesized conveniently according to Scheme 2 in MeCN. After reducing the volume of the reaction mixtures, the desired complexes were precipitated by the addition of THF. The purification was effectively achieved by re-dissolving the crude material in MeCN and precipitation by the addition of THF. This method was satisfactory to produce analytically pure complexes, cf. experimental part.

Structural descriptions

The mononuclear type **VI** *complexes* **4**–**9**: The solid state structures of these complexes were determined by single crystal X-ray crystallographic studies, whereby **5** forms crystals of the composition [^{n}Bu$_4$N]$_2$[Ni(opboEt$_2$)]·2H$_2$O (**5'**) and **8** forms [^{n}Bu$_4$N]$_2$[Cu(opboEt$_2$)]·2H$_2$O (**8'**). The molecular structures of the dianionic complex fragments of the Ni^{II}/Cu^{II} containing type **VI** complexes are shown in Figures 1 and 2, respectively, selected bond lengths and angles are given in Table 1 and crystal/ structural refinement data are summarized in Table 3. The dianionic complex fragments [M(opboR$_2$)]$^{2-}$ are denoted in the following as follows: M = Ni^{II}, R = Me (**4A**), Et (**5A**), ^{n}Pr (**6A**) and M = Cu^{II}, R = Me (**7A**), Et (**8A**), ^{n}Pr (**9A**).

For **6** the asymmetric unit comprises two crystallographically different [Ni(opbo(^{n}Pr)$_2$)]$^{2-}$ dianionic complex fragments, denoted as **6A** (comprising Ni1) and **6B** (comprising Ni2). Related bond lengths and angles of **6A** and **6B** show differences of up to ca. 2% and ca. 6%, respectively. Additionally, in case of **6A** an *anti*-conformation of the ^{n}Pr groups with respect to their orientation to the almost planar {Ni(opbo)} unit is observed, whereas for **6B** a *syn*-conformation is found. Despite this, only data of **6A** will be discussed. For completeness and comparison Table 1 gives bond lengths and angles of both **6A** and **6B**. Figure S1† displays the molecular structures of **6A** and **6B**. The 1D chains formed by **5'** and **8'** due to intermolecular hydrogen bonds are illustrated in Figures S2 and S3,† while selected bond lengths and angles of these hydrogen bonds are given in Tables S1 and S2, respectively.†

For **5A** and **8A** crystallographically imposed C_2 symmetry is observed. The C_2 axes pass the M1 atom and the middle of the C3/C3A bond, cf. Figure 1 and 2. In contrast, all other here discussed [M(opboR$_2$)]$^{2-}$ fragments exhibits C_1 symmetry. Moreover, as revealed from entries in Table 3, related pairs of Ni^{II}/Cu^{II} containing complexes (**4** and **7**, **5** and **8**, **6** and **9**) can be regarded as isomorphic to each other. In case of the related Ni^{II}/Cu^{II} pair of **6** (Ni^{II}, monoclinic, *P2(1)*) and **9** (Cu^{II}, monoclinic, *P2(1)/c*) unit cell parameters are in good agreement with each other, although the determined space group is different. It is verified, that a solution/refinement of **6** in the space group *P2(1)/c* and of **9** in *P2(1)*, respectively, is not possible. Responsible for this observation is the orientation of the ^{n}Pr groups with respect to the planar {M(opbo)} units, cf. above. Despite this, the isomorphism of corresponding pairs indicates that a co-crystallization of them should be possible, cf. experimental part.

A common feature of **4A–9A** is the coordination of the respective opboR$_2{}^{4-}$ ligands to the metal ions by their four deprotonated amido nitrogen atoms N1–N4, forming planar MN$_4$ coordination units, cf. Figure 1 and 2. The metal ions are located 0.004(1) Å (**4A**), 0.000 Å (**5A**), 0.006(5) Å (**6A**), 0.001(1) Å (**7A**), 0.0002(10) Å (**8A**) and 0.003(3) Å (**9A**), respectively, above/below of calculated mean plans of the atoms N1–N4 with root mean square deviations (rmsd) from planarity of 0.033 Å (**4A**), 0.047 Å (**5A**), 0.001 Å (**6A**) 0.055 Å (**7A**), 0.081 Å (**8A**) and 0.023 Å (**9A**), respectively. The planarity of the MN$_4$ coordination units is indicated further by the sum of the four bond angles around the metal ions of 360.05(14)° for **4A**, 360.14(17)° for **5A,** 360.0(7)° for **6A**, 360.18(14)° for **7A**, 360.41(16)° for **8A** and 360.1(6)° for **9A**, respectively. As observed and discussed for the related type **IV** complexes, cf. Scheme 1,[14] a unique feature of planar complexes possessing 5-5-5 fused chelate rings around the respective metal ion is, that three of the bond angles are rather small, whereas the fourth one is substantial larger. Indeed, this situation is

Fig. 1 ORTEP diagrams of the molecular structures of **4A**, **5A** and **6A** (left to right) at 50, 50 and 25 % ellipsoid probability. Above: Top view. Below: Side view. All hydrogen atoms are omitted for clarity.

The sign ⦨ refers to calculated interplanar angles between differently coloured mean planes. With hdp the atom having the highest deviation from planarity of calculated mean planes is indicated. Symmetry operation for 'A' **5A**: –x, y, –z + ½.

observed as well for **4A–9A** with the bond angles N1–M1–N3, N1–M1–N2 and N3–M1–N4 being in the range from 80.8(3)° (**9A**) to 86.3(4)° (**6A**) compared to the N2–M1–N4 bond angles in the range from 106.16(7)° (**4A**) to 112.38(11)° (**8A**).

The M–N bonds can be divided into M–N_{aryl} and M–N_{alkyl} bonds with respect to the substituents at the *N* donor atoms. Especially for Ni^{II}-containing **4A** and **5A** the M–N_{aryl} bond lengths (range: 1.8485(16) Å (**4A**) to 1.8546(15) A (**5A**)) are significantly shorter compared to the M–N_{alkyl} ones, although for **6A** and the Cu^{II}-containing complex fragments **7A–9A** this difference is not significant. The M–N_{aryl} bond lengths of **7A–9A** (range: 1.934(6) Å (**9A**) to 1.967(7) Å (**9A**) exceeds those of **4A–6A** (range: 1.8485(16) Å (**4A**) to 1.879(7) Å (**6A**)) dramatically, whereas a comparison of the M–N_{alkyl} bond lengths reveals minor differences only, cf. Table 1. Such differences have been observed for pairs of Ni^{II}/Cu^{II}-containing related type **IV** complexes as well and could be explained by the shorter ion radii of Ni^{II} (63 pm) compared to that of Cu^{II} (71 pm) in quadratic planar coordination environments.[15]
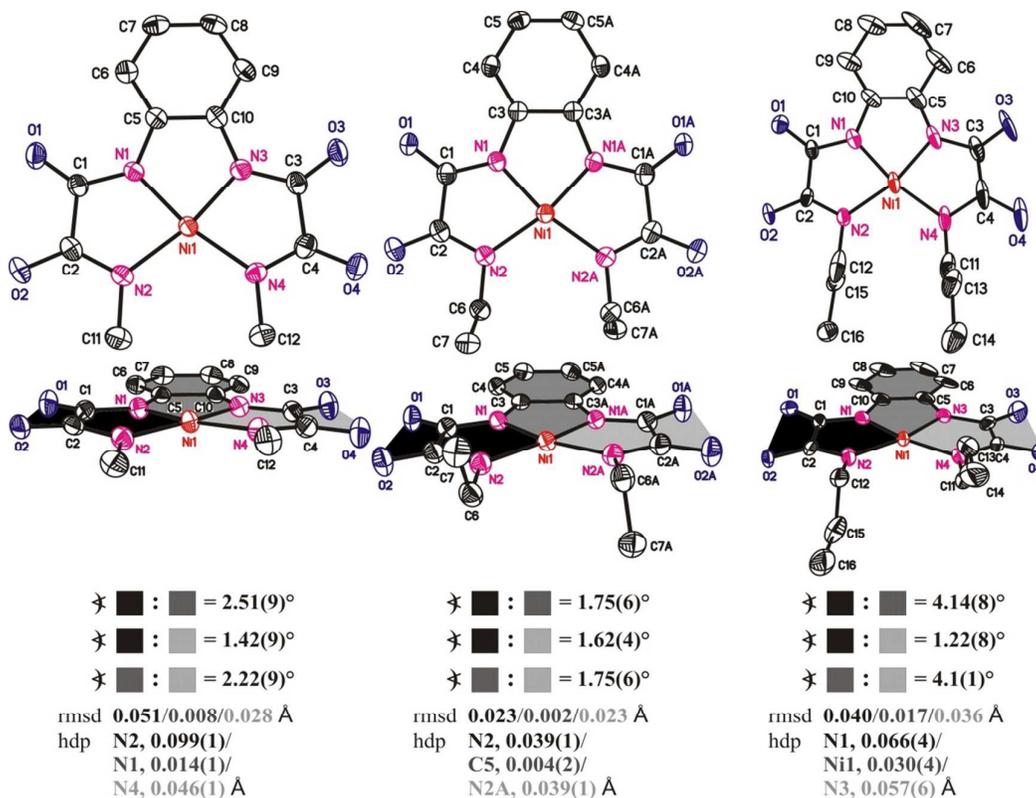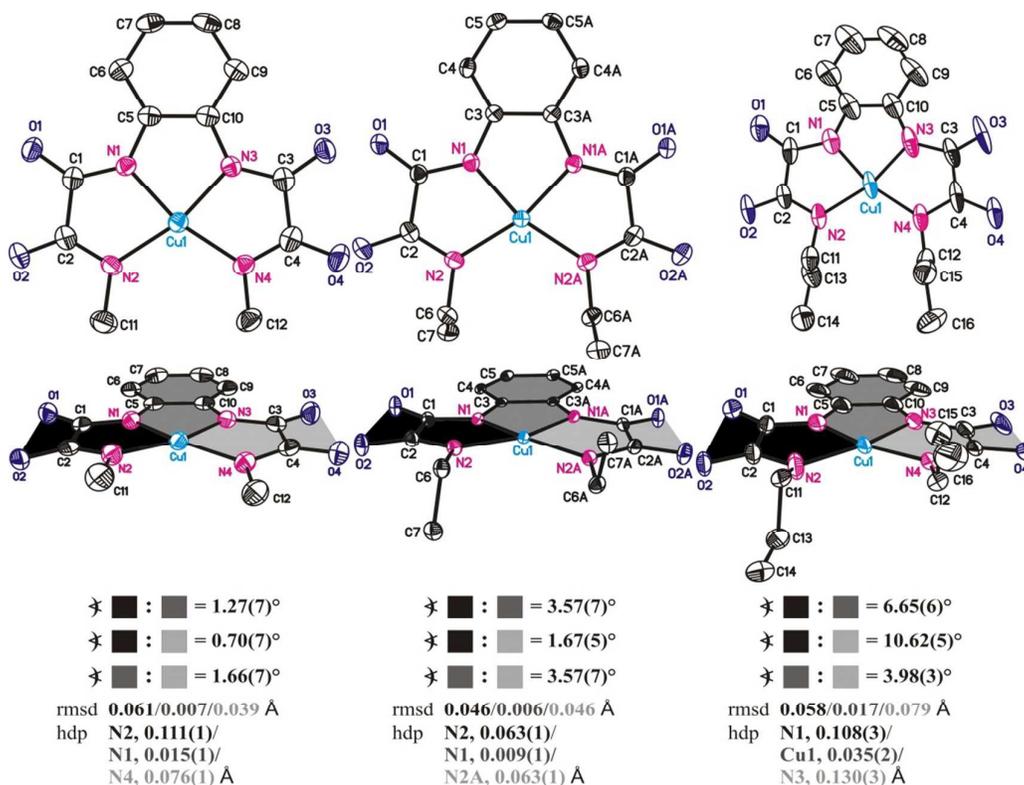

Fig. 2 ORTEP diagrams of the molecular structures of **7A**, **8A** and **9A** (left to right) at 50, 50 and 25 % ellipsoid probability. Above: Top view. Below: Side view. All hydrogen atoms are omitted for clarity.

The sign ⤩ refers to calculated interplanar angles between differently coloured mean planes. Symmetry operation for 'A' **8A**: –x, y, –z + ½.

*The trinuclear type **IX** complexes **10** and **12***: The solid state structures of the trinuclear type **IX** complexes **10'**, cf. experimental part and of **12** in form of $[Cu_3(opbo^nPr_2)(pmdta)_2](NO_3)_2 \cdot \frac{1}{2}CH_2Cl_2 \cdot ^3/_4Et_2O$ (**12'**), have been determined by single crystal X-ray crystallographic studies.

The molecular structures of the dicationic complex fragments $[Cu_3(opboR_2)(pmdta)_2]^{2+}$ of **10'** and **12'** (denoted in the following as **10A** and **12A**) are displayed in Figure 3. Selected bond lengths and angles of the $[Cu(opboR_2)]^{2-}$ and $[Cu(pmdta)]^{2+}$ fragments of **10A** and **12A** are given in Table 1 and 2, respectively. As described in the experimental part, the trinuclear and dicationic complex fragment **10A** has been refined as a whole disordered on two positions. Thus, the fragment with the major occupation factor is referred to as **10A**, the other as **10B**. In the following we will describe **10A** only, although Table 1 and 2 refer to data of both **10A** and **10B**. In Table 4 selected crystallographic and structural refinement data of **10'** and **12'** have been summarized.

The central Cu^{II} ions of **10A** and **12A** are all coordinated by four deprotonated amide *N* donor atoms to form CuN_4 coordination units. The CuN_4 units can be regarded as planar-quadratic, as calculations of mean planes of the N1–N4 atoms give the rmsd/hdp values as follows: **10A/12A** (rmsd, hdp) = 0.0005 Å, N1 with 0.0005(4) Å/0.004 Å / N1 with 0.086(7) Å, respectively, with the Cu1 atoms placed nearly in plane of the calculated N_4 mean planes (**10A**: 0.007(3) Å. **12A**: 0.008(7) Å). Additionally, the sum of bond angles of the CuN_4 units amounts to 360.0(6)° (**10A**) and 360.4(10)° (**12A**), which indicates the CuN_4 units as planar.

As observed and discussed for **4A–9A**, three bond angles of the CuN_4 units are rather small; whereas the fourth one is substantial larger as described for **7A–9A**, cf. above. This difference is not significant for **10A** and **12A**, cf. Table 1.
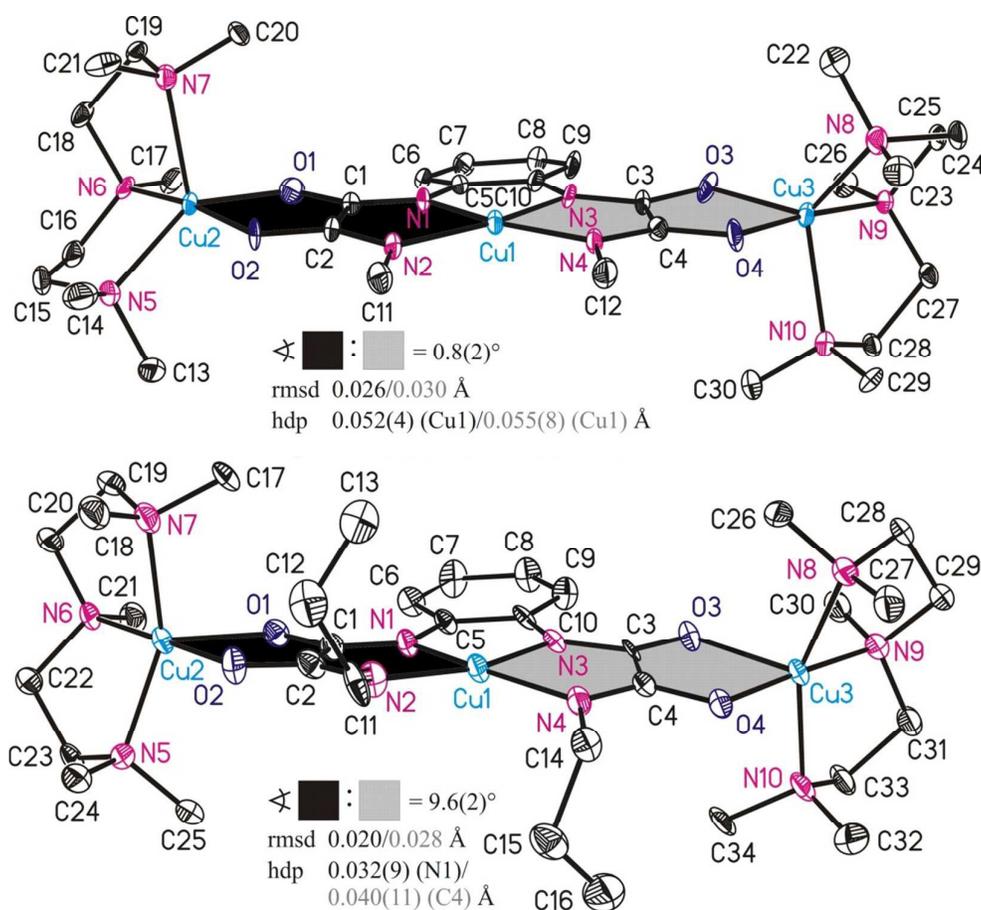
Fig. 3. ORTEP diagrams (25 % ellipsoid probability) of the molecular structures of **10A** (top) and **12A** (down). All hydrogen atoms are omitted for clarity. The sign ∡ refers to calculated interplanar angles between differently coloured mean planes.

The central CuN$_4$ units of **10A** and **12A** are obviously planar, although only the {Cu$_3$(opbo)} fragment of **10A** is planar in contrast to **12A**, cf. Figure 3. The deviation from planarity of the {Cu$_3$(opbo)} fragment of **12A** is not induced by the coordination of either counter anions and/or solvent molecules to the central Cu1 atoms. Indeed, for solvent free **10'** any coordination of the [BPh$_4$]$^-$ anions is certainly not expected. Even in case of **12'** no coordination of any specie to the central Cu1 atoms is observed. It should be mentioned additionally, that in the crystal structures of **10'** and **12'** no further intermolecular interactions are observed.

The terminal Cu^{II} ions of **10A** and **12A** are each coordinated by two O donor atoms of the respective oxamidato group as well as the three N donor atoms of the pmdta ligands, forming thus CuN$_3$O$_2$ coordination units. The geometries of these units are, with respect to their averaged τ parameters $<\tau>$,[16] cf. Table 2, closer to the ideal

trigonal-bipyramidal (**10A**) or to the ideal square-pyramidal coordination geometry (**12A**).

A further feature of these CuN_3O_2 coordination units needs to be discussed. For the related type **VIII** complex **14**[8a] it is observed, that the largest bond angle of the CuN_3O_2 unit at the "oxamidato side" involves the O donor atom of the $O\text{---}C\text{---}N_{alkyl}$ function and the middle N donor atom of the pmdta ligands. For the related CuN_3O_2 unit at the "oxamato side" the situation is different. Here, the largest bond angle involves the O donor atom of the $O\text{---}C\text{---}N_{aryl}$ function. This specific feature is furthermore usually observed for type **VII** complexes, as already explained along with the structural discussion of **14**.[8a] For **10A** and **12A** it is then exclusively observed, that the largest bond angles of the terminal CuN_3O_2 units involves the O donor atom of the $O\text{---}C\text{---}N_{alkyl}$ function and the middle N donor atom of the pmdta ligands, cf. Figure 3 and Table 2.

In summary it can be ruled out, that a replacement of the two O donor atoms involved in the coordination of the central Cu^{II} ions of type **VII** complexes by N(R) donor atoms to give the corresponding type **IX** complexes leads to such trinuclear{Cu_3(opbo)} fragments of which the central Cu^{II} ions are not coordinated by further co-ligands. Furthermore, this replacement rearranges the geometries of the terminal CuN_3O_2 units. Both observations compare well with the related type **VIII** complex **14**,[8a] although certainly additional work is required to figure out if they are universally valid.

Please, insert here Table 1

Please, insert here Table 2

Please, insert here Table 3

Please, insert here Table **4**

ESR spectroscopic investigations

The ESR experiments were performed in order to obtain information on the g-factors and the hyperfine (HF) coupling tensor of Cu^{II}, which are important for the discussion of magnetic properties of the complexes studied in this work, cf. below. The relevant interactions, which determine parameters of the Cu^{II} ESR spectrum, are standardly described by the following Hamiltonian:

$$H = g\mu_B B_0 S + S A^{Cu} I^{Cu} + \sum_{i=1}^{4} S A^{N_i} I^{N_i} + H_i \qquad (1)$$

Here, the first term represents the Zeeman interaction of an electron spin S with the external magnetic field B_0, whereas g and μ_B stand for the g-tensor and Bohr magneton, respectively. The HF interaction between the electron spin S of Cu^{II} and the ^{63}Cu, ^{65}Cu and ^{14}N nuclear spins I^{Cu} and I^N is described by the second and the third term, respectively. Here, A^{Cu} and A^N are the respective HF coupling tensors. Finally, H_i accounts for the nuclear Zeeman, hyperfine, and nuclear quadrupole interactions of further surrounding nuclei, like, e.g., protons.

The isotropic ESR parameters of **8** and **9** were obtained from measurements of 1 mM acetone solutions. In Figure 4 their ESR spectra are displayed together with performed simulations. The ESR spectra of both **8** and **9** appear rather similar. Both spectra consist of four lines due to the onsite HF coupling of the electron spin of Cu^{II} $S = \frac{1}{2}$ to its own nuclear spin I ($^{63, 65}Cu$) = $^3/_2$. From the modelling of the spectra, cf. Figure 4, the isotropic g-factor, the ^{63}Cu-HF coupling constants and the ^{14}N-HF coupling constants were obtained, respectively. Experimentally determined isotropic ESR parameters are listed in Table 5. We note that in this work in the model calculations of ESR spectra based on the Hamiltonian (1) we took into account only the HF interaction of the electron spin of copper with the spins of the nitrogen nuclei and neglect much weaker interactions with more distant nuclei (last term in (1)).

In order to obtain anisotropic ESR parameters, the angular dependence of the ESR spectra of a single crystal of **9@6** at f = 9.56 GHz at room temperature was measured by rotation of the magnetic field B_0 in the plane perpendicular to the molecular plane. For a single crystal of **8@5**, the extreme orientations of the spectrum corresponding to the principle axes of the g- and HF-tensors were determined by measuring the angular dependence of the g-factor by rotating around an arbitrary axis and searching the direction of B_0 for the minimum g-factor. This direction was chosen as a new axis, about which the angular dependence of the g-factor and HF-coupling constants were
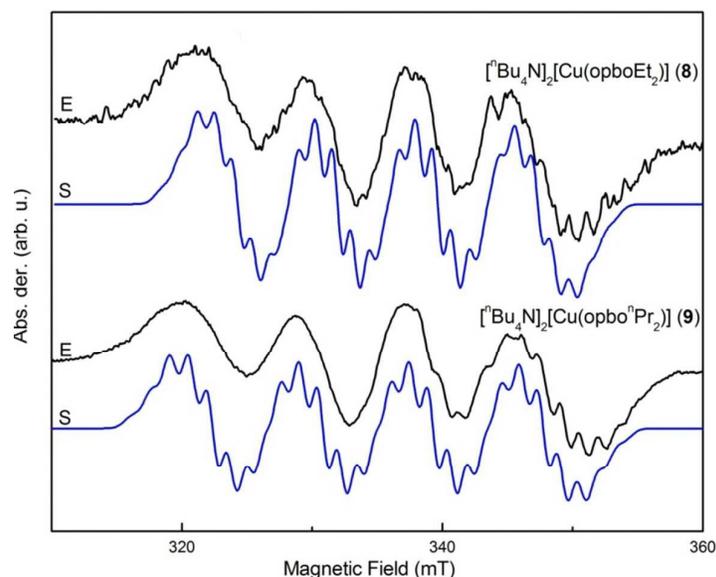
Fig. 4 Experimental (E) and simulation (S) X-band ESR spectrum of **8** (up) and **9** (bottom) in acetone at f = 9.8 GHz (X-band) at room temperature.

Table 5 Principal values of g, A^{Cu} (MHz) and A^{N} (MHz) of **8** and **9** from ESR measurements

Complex	$g_\perp$	g_{II}	g_{iso}	$A_\perp^{Cu}$	A_{II}^{Cu}	A_{iso}^{Cu}	$A_\perp^{N}$	A_{II}^{N}	A_{iso}^{N}
8	2.036	2.162	2.082	43.4	611	225.8	36.9	50.2	40.8
9	2.04	2.159	2.086	54.9	622.5	237.9	37.6	48.8	40.9

measured. Finally, to check the correctness of the procedure, the direction of the maximum g-factor was chosen as the rotation axis and indeed no angular dependence is found. In this experiment the spectra were recorded with a rotation interval of 15°. Representative ESR spectra of a single crystal of **8@5** and **9@6**, respectively, together with their simulation are shown in Figure 5.
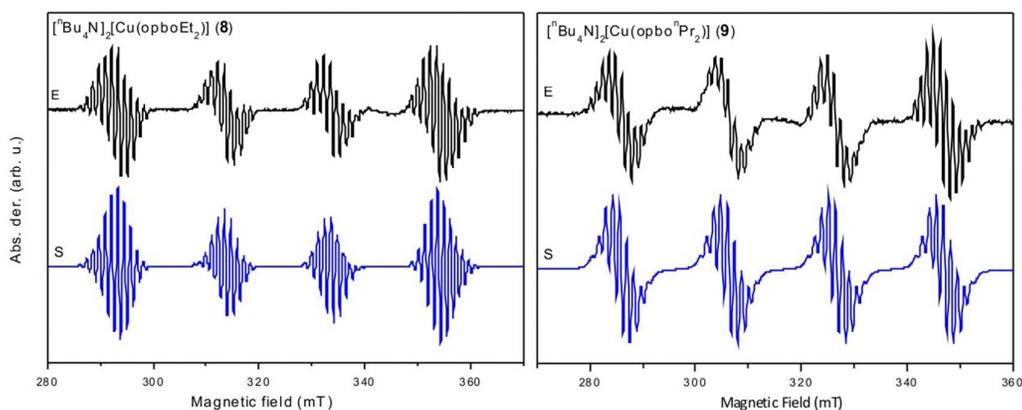

Fig. 5 Experimental (E) and simulation (S) X-band ESR spectrum of a single crystal of **8@5** (left) and **9@6** (right) at f = 9.56 GHz (X-band) at room temperature. The magnetic field is oriented parallel to symmetry axis of the CuN_4 unit, cf. Figure 6.

Both spectra consist of two quartet groups of lines owing to the HF-coupling with the $^{63,65}Cu$ nuclear spin I $(^{63,65}Cu) = {}^{3}/_{2}$. Each group further represents a subset of lines. They arise due to transferred HF-coupling with the ^{14}N nuclear spins I $(^{14}N) = 1$ of the four N donor atoms which can be, cf. Figure 6, classified in two equivalent groups. When the magnetic field is parallel to the normal of the molecular plane n $(B_0 \parallel n)$, the largest g value and the largest copper HF constant are obtained. The smallest g value is obtained when the magnetic field lies in the molecular plane $(B_0 \perp n)$. For this field geometry the line groups overlap because of the small ^{63}Cu-HF coupling constant $A_\perp^{Cu}$ in this direction. Therefore the extraction of the coupling parameters gets very difficult.
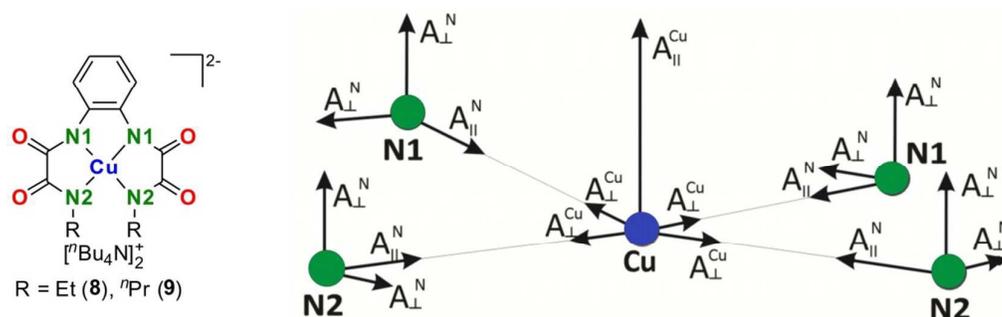
Fig. 6 Left: Chemical structure of studied complexes. Right: Scheme of the principal axes of the Cu and N hyperfine tensors of the CuN$_4$ unit.

Owing to the above described difficulties, the values of $A_\perp^{Cu}$ and A_{II}^{N} were estimated with the aid of the isotropic values using the relation $A_{iso}= (2A_\perp + A_{II})/3$. For the investigated complexes, the following assumptions are taken:

$$g_x = g_y = g_\perp, g_z = g_{II}, A_x = A_y = A_\perp < A_z = A_{II} \qquad (2)$$

Principal values of g, A^{Cu} and A^{N} of **8** and **9** obtained from modeling of the ESR spectra are listed in Table 5. In general, differences between values reported in Table 5 are not significant, the largest principal values for A^{Cu} were obtained for **9**.

Pulse ENDOR study

To obtain additional insights into the HF coupling, pulse Davies ENDOR experiments were performed on a single crystal of **8@5**. In Figure 7 experimental and simulated ENDOR spectra at different orientations of the crystal in the magnetic field are shown. The 0° orientation corresponds to the direction of B_0 along the g_{II} - axis of the g-tensor, and the 90° orientation represents the perpendicular direction. The measurements were carried out at the magnetic field value corresponding to the

position of the second from the left group of lines in the CW spectrum (~ 310 mT), cf. Figure 5. In the ENDOR spectra, peaks both from the nitrogen nuclei as well as from protons (^{1}H) can be identified. The latter ones are located at the low frequency part of the spectrum and are marked correspondingly in Figure 7. They were not considered in the modeling of the ENDOR spectra. Despite an appreciably lower single-to-noise (S/N) ratio of the ENDOR spectra as compared to the ESR spectra, the peaks of the individual nitrogen nuclei are quite well resolved.

The principal axes of g and A^{Cu} coincide with their maximum components located perpendicular to the molecular plane. The maximum components of the ^{14}N hyperfine tensors were found to lie parallel to the Cu–N bond vectors as sketched in Figure 6. The principle values of g, A^{Cu}, and A^N obtained from the ENDOR measurements are shown in Table 6. They agree reasonably well with the ESR data, cf. Table 5. Note that, unlike in the ESR experiment, the better resolution of the ENDOR method enables, with the help of the modeling of the spectra on the basis of (1) and (2), to estimate all four nitrogen HF tensors. They are presented in Table 6 and labeled as **A**, **B**, **C** and **D**. In agreement with the ESR results, $\left| A_{\perp}^N \right| < \left| A_{II}^N \right|$ has been found for all
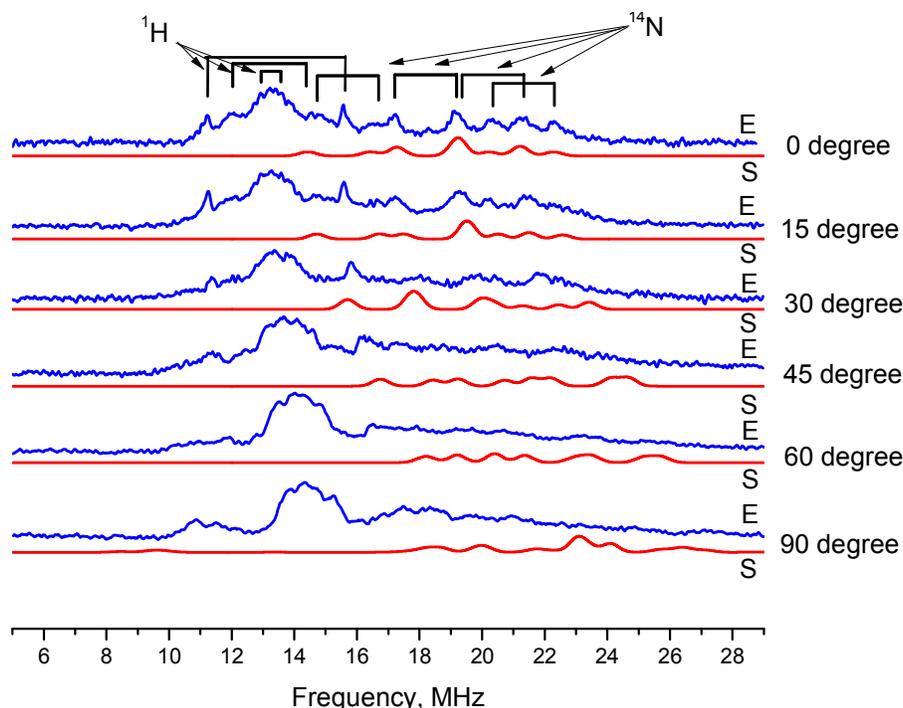

Fig. 7 Experimental (E) and simulated (S) Davies-ENDOR spectra of **8@5** (X-band, T = 20 K) at six different orientation of the single crystal in the external magnetic field. The 0° orientation corresponds to the direction of B_0 along the $g_{\parallel}$ axis of the g tensor, and the 90° orientation represents the perpendicular direction.

four tensors. With the parameters listed in Table 6 a satisfactory agreement with experimental ENDOR spectra has been achieved. Most optimal fits were obtained close to the orientation of the magnetic field parallel to the normal to the molecular plane, which is due to a better S/N ratio for this field geometry. Considering the data in Table 6, the nitrogen HF tensors can be grouped in pairs **A-B** and **C-D** with quite close values of the tensor components in each group, respectively. However, the ENDOR measurements indicate some difference in the HF parameters within each group, which is not evident in the static ESR data. The difference of the HF parameters between the two groups is substantial. The larger values of the HF constants of the group **A-B** enable to tentatively assign them to the N1 labeled N_{aryl} donor atoms, cf. Figure 6, since these values are closer to those of related type **IV** Cu^{II}-containing bis(oxamato) complexes comprising only two N_{aryl} donor atoms.[10] The smaller HF constants in the group **C-D** can then be associated with the N2 labeled N_{alkyl} donor atoms, cf. Figure 6.

Table 6 Principal values of g, A^{Cu} (MHz), and A^{N} (MHz) of **8** from an ENDOR measurement

$g_{\perp}$	g_{II}	$A_{\perp}^{Cu}$	A_{II}^{Cu}
2.016	2.144	49	639

	A	**B**	**C**	**D**
A_{II}^{N}	51.2	51.8	42.2	41.6
$A_{\perp}^{N}$	40.4	42.6	36.6	30.8

Analysis of the HF tensors

Two models introduced by Maki and McGarvey[17] and Morton and Preston[18] were used to calculate the spin density from experimentally obtained HF coupling constants of Cu^{II} ions and N donor atoms. According to Maki and McGarvey,[17] the Cu-HF coupling constants can be expressed as:

$$A_{II} = P\left(-\kappa - \frac{4}{7}\alpha^2 + \Delta g_{II} + \frac{3}{7}\Delta g_{\perp}\right) \qquad (3)$$

$$A_{\perp} = P\left(-\kappa + \frac{2}{7}\alpha^2 + \frac{11}{14}\Delta g_{\perp}\right) \qquad (4)$$

In these expressions $P\kappa$ is the Fermi contact term with $P(^{63}Cu) = \mu_B g_e \mu_n g_n \times \langle r^{-3} \rangle =$ 1164 MHz, that is the dipolar HF coupling parameter of the unpaired electron,[19] and $\Delta g_{\parallel,\perp} = g_{\parallel,\perp} - 2.0023$. The parameter α^2 is a covalency parameter, which describes the in plane metal–ligand σ bonding. The value of α^2 can be determined by using equations 3 and 4, cf. above, and the experimental Cu-HF coupling constants. The following normalization condition was used to determine α':

$$(\alpha^2 + \alpha'^2 - 2\,\alpha\,\alpha'\,S = 1) \qquad (5)$$

For the complexes under study, the α^2 and $(\alpha'/2)^2$ values are given in Table 7. The values of α^2 and $(\alpha'/2)^2$ represent then the spin density on the Cu^{II} ion (ρ_{Cu} (total)) and on the N-donor atom (ρ_N(total)), respectively.

Furthermore, the values obtained for the spin density on the Cu^{II} ion were compared with those deduced by the procedure of Morton and Preston.[18] This approach was also used to calculate the spin density on the N donor atoms. According to this approach, the spin density $\rho(s)$ and $\rho(p)$ on the s and p orbitals (d orbitals for Cu) are proportional to the isotropic or Fermi contact contribution A_{iso} and the dipolar HF coupling constant $A_{dip} = A_{iso} - A_{\perp}$, respectively. The proportionality constants for many abundant nuclei can be found in the literature.[18] Spin densities calculated according to Morton and Preston[18] are reported as well in Table 7. A more detailed description of these two models can be found in our previous work and Table 7 refers then additionally to corresponding data obtained for **13** and [^{n}Bu$_4$N]$_2$[Cu(opba)] (**15**).[8a,10] To make a direct comparison possible, the spin densities on the s orbital of the N donor atom of **13** and **15** are recalculated with the isotropic N HF coupling constant for unit spin density taken from ref 18.

Very similar spin densities on the Cu^{II} ion and N donor atoms of **8** and **9** are obtained, cf. Table 7. As observed earlier for **13**[8a] and **15**[10], the unpaired electron is mainly localized on the Cu^{II} ion in both **8** and **9**. Additionally, the averaged spin density on one individual N donor atom of **8** and **9** compares with that for **13**[8a] and **15**[10]. However, experimentally obtained data reported here for **8** and **9** do not follow the expected tendency, that a replacement of O versus N donor atoms results in a lower spin density on Cu^{II} and higher spin densities on the N donor atoms[9] when comparing with **13**[8a] and **15**[10], *vide infra*.

Table 7 Spin density (in %) for Cu and N of **8** and **9** in comparison with **13**[8a] and **15**[10].

Complex	$\rho_{Cu}{}^{a}$(total) $= \alpha^2$	$\rho_{Cu}{}^{b}$(total)	$\rho_{N}{}^{b}$(total)	$\rho_{N}{}^{b}$(s)	$\rho_{N}{}^{b}$(p)	$\rho_{N}{}^{a}$(total) $= (\alpha'/2)^2$
8	74	57.1	9.3	2.25	7.02	8.9
9	74	57.4	8.2	2.26	5.94	8.9
13[8a]	68	51	9.5	2.3	7.2	10.5
15[10]	71	54.6	14.5	2.5	12	10.3

[a] According to eqs 2, 3 and 4. [b] According to ref 18.

Furthermore, since ENDOR measurements on **8@5** have enabled to resolve individual HF tensors **A**–**D** of the *N* donor atoms, the spin density on them was estimated according to the approach by Morton and Preston[18]. The respective values are listed in Table 8.

Table 8 Spin density (in %) for the *N* donor atoms of **8** derived[18] from an ENDOR measurement

A			B			C			D		
ρ(s)	ρ(p)	ρ(total)	ρ(s)	ρ(p)	ρ(total)	ρ(s)	ρ(p)	ρ(total)	ρ(s)	ρ(p)	ρ(total)
2.43	6.48	8.91	2.52	5.58	8.1	2.12	3.42	5.54	1.9	6.48	8.38

One might expect the larger HF parameters of tensors **A**–**B** as compared with **C**–**D** to be reflected in larger spin densities ρ. This expectation is only partially met, since the value of ρ(total) for **D** appears the same as for **A**–**B**. Most likely this is related to a limited accuracy of the ENDOR experiment for the field direction close to the molecular plane, which has led to an overestimate of the anisotropy $(A_{\parallel} - A_{\perp})$ of tensor **D** and consequently to an overestimate of the partial spin density on the p orbital ρ(p). To remind, in the model of Morton and Preston[18] ρ(p) is directly proportional to $(A_{\parallel} - A_{\perp})$. Remarkably, the partial spin density on the s orbital ρ(s), which is determined by the isotropic part of the HF coupling $A_{iso} = (A_{\parallel} + 2A_{\perp})/3$, is similar for **C** and **D** and both are smaller compared to **A** and **B**, as expected.

Generally, the spin density on each *N*-donor atom, as estimated from ESR and ENDOR data is smaller than those obtained from DFT calculation. However, an inequality of the HF tensors obtained from the ENDOR measurement is compatible with the DFT calculation data based on the structural data from crystallographic characterization and yield different spin densities on all four *N*-donor atoms, cf. below. Apparently, the different spin densities on the *N* atoms reflect their different local geometries, as revealed by different HF tensors.

Magnetic properties

The temperature dependence of the inverse static magnetic susceptibility $\chi_m^{-1} = H/M$ of **10**–**12** together with the corresponding $\chi_m T$ dependence are presented in Figure 8. The $\chi_m^{-1}(T)$-dependence shows a strong non-linearity at T below 100 K which is typical for an antiferromagnetic interaction between the spins, see, e.g ref. [20]. The experimental data were fitted on the basis of the following Hamiltonian using the simulation software package julX:[21]

$$H = \sum_{i=1}^{3} \mu_B g_i B_0 S_i + J_{12} S_1 S_2 + J_{13} S_1 S_3 \qquad (6)$$

Here J_{12} and J_{13} denote the exchange integrals between the central and the terminal Cu^{II} spins and the first term stands for the Zeeman interaction. The values of J_{23} (the exchange integral between the two terminal Cu^{II} ions) in all investigated complexes were assumed to be negligibly small due to the large distance between the Cu2 and Cu3 atoms, cf. Figure 3, and the large number of orbitals involved in the corresponding super exchange interaction between them. The analysis yields the best possible fit with the values $J_{12} = J_{13}$ as shown in Figure 8.

The J values of the type **IV** complexes **10**–**12** are with –96 to –132 cm^{-1}, cf. Figure 8, are comparable with and even slightly larger in magnitude than J values of related type **VII** complexes as, for example, for **16/17** (–89 cm^{-1}/–111 cm^{-1})[11,12] and those of **14** (–130 cm^{-1}),[8b] a type **VIII** complex. As according to Kahn[9] and also others[22,23] a substitution of electronegative oxygen atoms vs. less electronegative nitrogen atoms should result in increased J couplings, the question arises whether the in magnitude somewhat larger J values reported here for the type **IV** complexes **10**–**12** as compared with related type **VII** complexes are due to this mechanism. We will continue this discussion after displaying next results obtained of accompanied DFT studies.
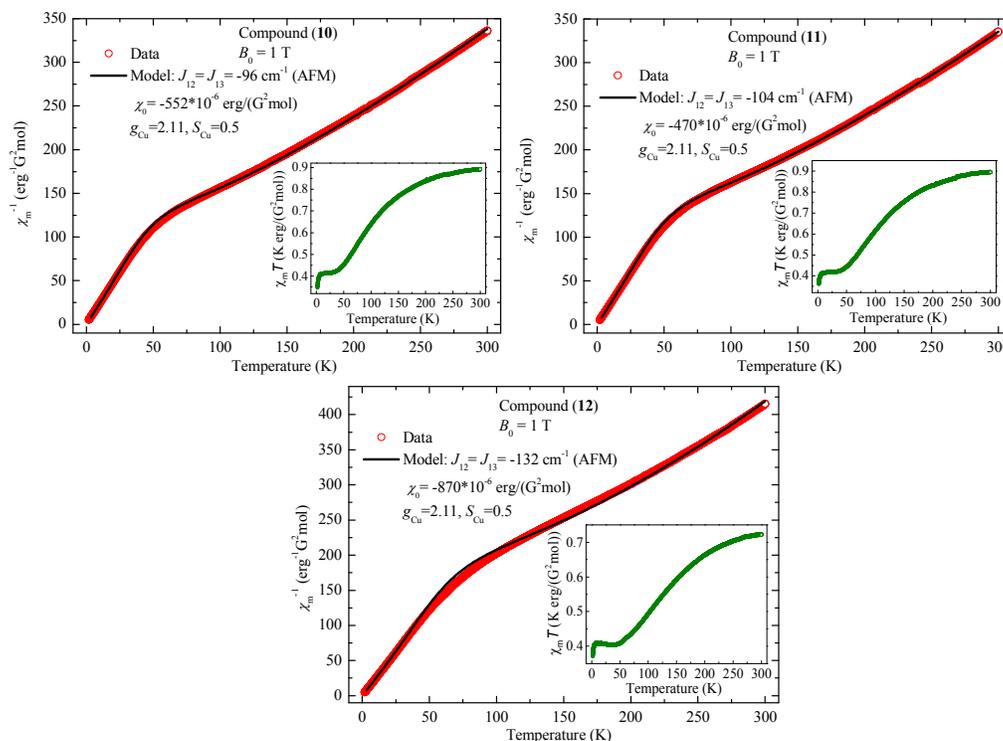
Fig. 8 Temperature dependence of the inverse magnetic susceptibility χ_m^{-1} of **10**–**12.** Symbols represent experimental data and solid lines correspond to the fitting results (see the text). Inset: plot of $\chi_m T$ as a function of T.

DFT calculations

Quantum chemical methods as specified in the Experimental Section were used to optimize the geometries of the dianionic complex fragments of **7A**–**9A**. Selected bond lengths and bond angles of thus obtained optimized complex fragments, now denoted as **7A**^{calc}–**9A**^{calc} are summarized in Table S3 in comparison with related data of **7A**–**9A**. Furthermore, Figure S4 displays the geometries of **7A**^{calc}–**9A**^{calc} in analogy as shown for **7A**–**9A** in Figure 2, cf. above. Beside an elongation of the bond lengths of the CuN$_4$ units of **7A**^{calc}–**9A**^{calc} compared to those of **7A**–**9A**, cf. Table S3, no mentionable differences of other related bond lengths and even of related bond angles is observed. It should be emphasized that an elongation of the bond lengths of the CuN$_3$O unit of geometry optimized dicationic **13A** compared to data of **13A** from crystallographic characterization has been already noticed by us.[8a] As observed for **7A**–**9A**, cf. Figure 2, even **7A**^{calc}–**9A**^{calc} cannot be considered as planar, cf. Figure S4, although deviations from planarity appear less dramatic.

Second, the spin density distribution of **7A**–**9A** and **7A**^{calc}–**9A**^{calc} were calculated and obtained values are given in Figure 9. It's to notice, that related N donor atoms of **7A**,

8A and/or **9A** do not have identical spin populations. For example, for the N_{aryl} donor atoms of **7A** values of 14.7 and 14.0 were calculated as given in Figure 9. Such differences are not observed for **7A**^{calc}–**9A**^{calc}. The differences observed for **7A–9A** are then attributed to distortions of the molecular geometries, as outlined above. Additionally, it's to notice that generally the spin population at the N donor atoms of **7A–9A** is larger compared to related atoms of **7A**^{calc}–**9A**^{calc}, whereas the spin population of the Cu atoms is smaller, cf. Figure 9. That is most probably due to overemphasizing long Cu–N bond lengths of **7A**^{calc}–**9A**^{calc}. Eventually, we do not aim to stress this point too much as corresponding data deviate by less than 10 %. In the following we refer, however, to calculated data of **7A**^{calc}–**9A**^{calc} only.

spin density at	7A		8A		9A		13[8]		15[10]	
	calc.[a,b]	exp.[a,c]	calc.[a,b]	exp.[a,c]	calc.[a,b]	exp.[a,c]	calc.[d]	exp.[c]	calc.[d]	exp.[c]
Cu	52.5/51.1	-	52.2/51.0	74/57.1	52.0/50.5	74/57.5	53.9	68/51	55	71.0/54.6
N_{aryl}	13.7$^{I/II}$/14.7^I,14.0^{II}	-	13.8$^{I/II}$/14.7^I,13.9^{II}	8.9/9.3	13.8$^{I/II}$/14.4^I,14.0^{II}	8.9/8.2	11.8^I,14.8^{II}	10.5/9.5	15	10.3/14.5
O/N_{alkyl}	8.9/8.4^{II}	-	8.8$^{I/II}$/9.1^I,8.7^{II}	8.9/9.3	8.8$^{I/II}$/9.4^I,9.2^{II}	8.9/8.2	7.7,8.8	10.5/9.5	7	10.3/14.5
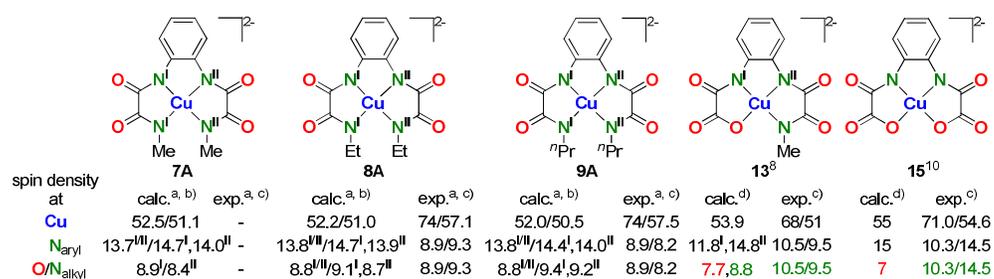
[a] This work. [b] First/second entry refer to data obtained for geometry optimized complex fragments or to data obtained by using complex geometries from crystallographic characterization, respectively. [c] The first/second entry refers to data obtained according to the approaches by Maki and McGarvey[17]/Morton and Preston[18]. [d] Data refer to geometry optimized fragments only. For further data of **13** cf. ref. [8].

Fig. 9 Selected values of the calculated and experimentally obtained spin population of **7A–9A** together with corresponding values of **13**[8a] and **15**[10].

It is certainly of interest to compare the spin density distribution of **7A–9A** with those already reported for **13**[8a] and **15**[10], as done in Figure 9. With respect to calculated values one can infer from Figure 9 that the change of the CuN_2O_2 unit of **15**[10] by a CuN_3O unit of **13**[8a] and finally by a CuN_4 unit of **7A–9A** results in a decrease of the remaining spin population at the Cu atoms (**15**: 55 %, **13**: 53.9, **7A–9A**: 52.2 % in average). This tendency could be expected, as according to Kahn the performed heteroatom substitution should result in a better overlap between the N donor atom orbitals to Cu compared to O donor atom orbitals.[9] That tendency is, however, not reflected by a clear trend in the spin population at the donor atoms of the Cu atoms. For example, for **15**[10] a spin population at the N_{aryl} donor atoms of 15 % was calculated, whereas for the N_{aryl} donor atoms of **7A**^{calc}–**9A**^{calc} this value amounts to ca. 13.8 %, cf. Figure 9. Nevertheless, the described tendency for the spin population at the Cu atoms agrees with the expectation. In case that there is an interplay between

the spin density distribution of mononuclear complexes as those in Figure 9 and J values of their corresponding trinuclear complexes, this tendency would indicate higher J coupling for corresponding trinuclear complexes of **7A–9A** compared to related complexes of **13**[8a] and **15**[10].

Finally, the calculated spin density distribution of **7A–9A** should be compared with the estimates from the HF tensors. As reported before,[8a] the experimental approach according to Morton and Preston[18] compares much better with calculated values as the Maki and McGarvey approach,[17] cf. Figure 9. Certainly, the differences of the spin population at the Cu atoms of **8A/9A** determined from the HF tensors and calculated values (exp. vs. calc. for **8A/9A** = 57.1/57.5 vs. 52.2/52.0) are larger than the difference reported for **13**[8a] (51 vs. 53.9) and **15**[10] (54.6 vs. 55). This could be related to simplifications implicit in the experimental approaches[17,18] which do not properly account for real local geometries of the complexes under question. In the approach of Maki and Macgarvey[17], the anisotropic HF coupling constants are calculated for a square planer molecular geometry. In the approach of Morton and Preston[18], the HF coupling constants are calculated for a free atom. For both models, this sets a limitation for obtaining precise spin density values due to a deviation from the square planer geometry for the complexes under study. Nevertheless, they still remain reasonable qualitative approaches to obtain insight into the spin density distribution of Cu^{II}-containing type **VI** complexes. Furthermore, calculated spin densities of **8A/9A** are different when compared to **8A**^{calc}/ **9A**^{calc}, cf. Figure 9, due to different geometries. The geometry of **8A** in **8@5** and of **9A** in **9@6** cannot be determined, but it seems likely that both **8A** and **9A** do not have identical geometries inside the diamagnetic diluted materials as determined by their crystallographic characterization. Thus, the observed differences of the calculated spin density distribution of **7A–9A** compared with those estimated from the HF tensors might be attributed to this effect as well.

Considering that the ESR spectra of type **VI** complexes as reported here are much more complicated compared to type **IV** and also type **V** complexes, the spin densities estimated from ESR and calculated spin density distribution reasonably complement each other. Moreover, the inequality of N donor atoms revealed for **8** in the ENDOR experiment, cf. above, is in good qualitative correspondence with the DFT results. Nevertheless, there remains the question if the increase of the exchange interaction in type **IX** complexes compared to type **VII** complexes is related to a smaller electronegativity of N donor atoms. This will be briefly discussed next.

Discussion

Before starting a discussion it should be pointed out, that from the experimental determination of the electron density distribution[23] and the assignment of spin density maps[22], respectively, of the ferrimagnetic chain complex $[\{MnCu(pba)(OH)\cdot 2H_2O\}_n]$ the magnetic coupling path of bis(oxamato) type complexes was aimed to be assigned. However, precise statements on the magnetic coupling path were not derived, although it is at least implied that the $N \doteq C \doteq O$ unit of the C_2NO_3 containing oxamato bridge contributes to a larger extent to the magnetic superexchange coupling compared to the $O \doteq C \doteq O$ unit.[22,23] Certainly, polymeric $[\{MnCu(pba)(OH)\cdot 2H_2O\}_n]$ compares marginally with the situation to be discussed here.

Unfortunately, **10** and **11** cannot be included in the following discussion. In case of **10** this is due to the isolation as "$[Cu_3(opboMe_2)(pmdta)_2](NO_3)_2$", of which the magnetic properties were measured. As this material could not be characterized crystallographically, it was converted into "$[Cu_3(opboMe_2)(pmdta)_2](BPh_4)_2$ (**10'**)" of which crystals were suitable for crystallographic studies. Compound **10'** displays then the same connectivity and coordination mode of the terminal Cu(pmdta) fragments as observed for **12**. However, due to the use of BPh_4^- anions in case of **10'** compared to NO_3^- anions in case of **10** especially bond angles are expected to be modified by, for example, packing effects. Of **10'** itself only very little quantities could be obtained. On the other hand, crystals of **11** were not suitable to determine the structure reliably, *vide supra*.

To identify the reason why the *J* values of type **IX** complexes exceed those of type **VII** complexes the following test should be instructive: Supposing that the formerly established nearly linear relationship between *J* values and τ parameters of type **VII** complexes[16,24] applies to corresponding type **IX** complexes as well, one could abstract the *J* value of **12** from Figure 10 with -112 cm^{-1}. To that *J* value we refer from now on as J_{abs}. The experimentally determined *J* value of **12** with -132 cm^{-1} exceeds than J_{abs} significantly. Out of that observation one could already conclude that for the same τ parameter *J* values of type **IX** complexes are larger when compared to type **VII** complexes, although the solid line in Figure 10 displays an average estimate for type **VII** complexes. Additional support comes then from the calculated spin density distribution of especially **9A** as precursor of type **IX 12** compared to **15**[10] as precursor of type VII **16**.[11] Thereby, the Cu atom of **9A**^{calc} exhibits a spin density of 52.0 %
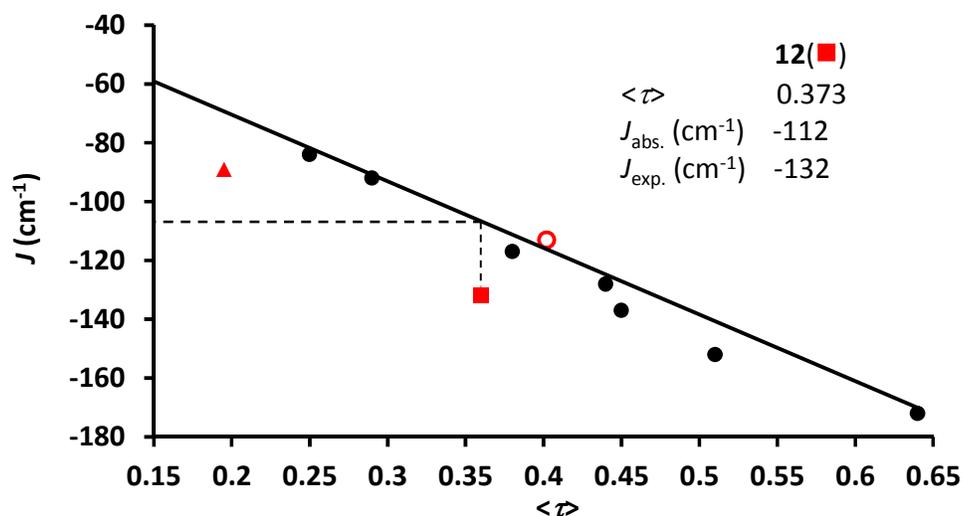
Fig. 10 Representation of the experimentally determined J values of **16** ($\blacktriangle$),[11] $[Cu_3(nabo)(pmdta)_2(BF_4)](BF_4)\cdot MeCN\cdot Et_2O$ (nabo = 2,3-naphtalene-bis(oxamato)) ($\circ$)[11] and **12** ($\blacksquare$) vs. its $<\tau>$ parameters of the terminal Cu^{II} ions in comparison with values of related type **VII** complexes.[16,24]

compared to 55 % calculated for **15**.[10] This striking difference could indeed be a consequence of the replacement of the O donor atoms of **15** by less electronegative N donor atoms in **9A**, as proposed by Kahn.[9]

Unfortunately, up to now with **12** only one crystallographically characterized type **IX** complex can be described, of which the magnetic properties were determined. Due to that it is not yet possible to conclude if type **IX** complexes exhibit a related linear J versus τ dependence as observed for type **VII** complexes,[16,24] keeping in mind that the bonding situation of the terminal CuN_3O_2 units is different. That different bonding situation of type **IX** versus **VII** complexes might then have an impact on the magnetic superexchange coupling path, which cannot be ruled out here and points out that additional work is required.

Summary and Conclusions

Starting from the <u>o</u>-phenylene<u>b</u>is(N(R)-<u>ox</u>amides) (opboH$_4$R$_2$, R = Me **1**, Et **2**, ^{n}Pr **3**), achieved in good yields, the corresponding mononuclear Ni^{II} and Cu^{II} complexes in form of their tetrabutylammonium salts [^{n}Bu$_4$N]$_2$[M(opboR$_2$)] (M = Ni, R = Me **4**, Et **5**, ^{n}Pr **6**; M = Cu, R = Me **7**, Et **8**, ^{n}Pr **9**) could be successfully synthesized. Out of **7**–**9** the trinuclear bis(oxamidato) type complexes [Cu$_3$(opboR$_2$)(L)$_2$](NO$_3$)$_2$ (L = pmdta, R = Me **10**, Et **11**, ^{n}Pr **12**) could be obtained and characterized by, for example, single crystal X-ray diffraction studies in form of [Cu$_3$(opboMe$_2$)(pmdta)$_2$](BPh$_4$)$_2$ (**10'**) and [Cu$_3$(opbo^{n}Pr$_2$)(pmdta)$_2$](NO$_3$)$_2 \cdot$½CH$_2$Cl$_2 \cdot ^3/_4$Et$_2$O (**12'**).

ESR studies of **8**@*5* and **9**@*6* allowed an estimation of the spin density distribution of **8A** and **9A** by two different approaches. Single crystal ENDOR measurements of **8**@*5* have enabled to resolve individual spin densities of the four N donor atoms of **8A** as individual HF tensors could be observed. The spin densities estimated from HF tensors agree fairly when compared with quantum chemically calculated ones. Especially the inequality of the HF tensors obtained from the ENDOR measurement of **8**@*5* compares well with calculated spin densities of the N donor atoms of **8A** in case that the crystallographically determined geometry of **8A** is applied for calculation. These results proof at least that the spin densities of the two different types of N donor atoms of **8A/9A**, namely the N_{aryl} and N_{alkyl} type atoms, are significantly different.

Out of susceptibility measurements versus temperature the J parameters of the trinuclear Cu^{II}-containing bis(oxamidato) complexes (type **IX** complexes) **10** (–96 cm^{-1}), **11** (–104 cm^{-1}) and **12** (–132 cm^{-1}) have been determined. They appear larger in magnitude when compared to J values of reported type **VII** complexes.[1] Our discussion of the spin density distribution favours the scenario that the enhancement of the exchange coupling J is related to the substitution of the O donor atoms in complexes of type **VII** by less electronegative N donor atoms in complexes of type **IX**. To this end, the present work supports earlier studies,[8a,10] in which an interplay between the spin density distribution of mononuclear type **IV** and **VI** complexes and magnetic superexchange interactions of trinuclear complexes derived out of them has been proposed.

Experimental section

General methods and materials

All chemicals were purchased from commercial sources and used as received without further purification. The solvents were purified according to standard procedures.[25] NMR spectra were recorded at room temperature with a Bruker AvanceIII 500 Ultra Shield Spectrometer (^{1}H at 500.300 MHz and ^{13}C$\{^1$H$\}$ at 125.813 MHz) in the Fourier transform mode. Chemical shifts are reported in δ (ppm) vs. SiMe$_4$ with the solvent as the reference signal ([D$_6$]-DMSO: ^{1}H NMR, $\delta = 2.54$; and ^{13}C$\{^1$H$\}$NMR, $\delta = 40.45$). FT-IR spectra were recorded in the range of 400–4000 cm^{-1} on a Perkin-Elmer Spectrum 1000 FT-IR spectrophotometer as KBr pellets. Elemental analysis for C, H and N were performed on a Thermo FlashAE 1112 series. The diethyl ester of *N,N'-o*-phenylene-bis(oxamic acid) (opbaH$_2$Et$_2$),[26] compounds **1–3**,[3] and [Cu(pmdta)(NO$_3$)$_2$][27] were synthesized according to published procedures.

Synthesis of [^{n}Bu$_4$N]$_2$[Ni(opboR$_2$)], R = Me (4), Et (5), ^{n}Pr (6).

A hot solution (*ca.* 50 °C) of [Ni(OAc)$_2$(H$_2$O)$_4$] (0.49 g, 0.002 mol) in MeOH (50 mL) was added dropwise with stirring to a hot suspension (*ca.* 50 °C) of **1**, **2** or **3** (0.002 mol), respectively, in MeOH (50 mL). Then, ^{n}Bu$_4$NOH (5.18 g, 40% in MeOH, 0.008 mol) was added with continuous stirring. The resulting mixture was stirred at 60 °C for further 15 minutes, filtered and the solvent evaporated to dryness. The resulting oily material was treated with THF (25 mL) and filtered to eliminate [^{n}Bu$_4$N]OAc. The desired complex was precipitated by addition of Et$_2$O (200 mL), as orange powder, filtered and dried in *vacuo*. Figures S5–S7† give the ^{1}H NMR and IR spectra of **4–6**, respectively.

4. Yield: 1.32 g (81%). Anal. calcd (%) for **4** (C$_{44}$H$_{82}$N$_6$NiO$_4$, 817.85 g mol^{-1}): C 64.62, H 10.11, N 10.28; Found: C 64.02, H 10.59, N 9.88. IR: $\nu = 2959$(m), 2870(m) (CH); 1622(s), 1589(s), 1576(s) (CO). ^{1}H NMR: $\delta = 0.94$ (t, 24H, H^a), 1.36 (m, 16H, H^b), 1.57 (m, 16H, H^c), 2.39 (s, 6H, H$^{1,1'}$), 3.15 (t, 16H, H^d), 6.43 (dd, 2H, H$^{6,6'}$), 7.95 (dd, 1H, H$^{5,5'}$).

5. Yield: 1.25 g (74%). Anal. calcd (%) for **5** (C$_{46}$H$_{86}$N$_6$NiO$_4$, 845.91 g mol^{-1}): C 65.31, H 10.25, N 9.93; Found: C 64.96, H 10.40, N 9.90. IR: $\nu = 2958$(m), 2872(m) (CH); 1619(s), 1587(m), 1572(s) (CO). ^{1}H NMR: $\delta = 0.87$ (t, 6H, H$^{1,1'}$), 0.94 (t, 24H,

H^a), 1.31 (m, 16H, H^b), 1.57 (m, 16H, H^c), 2.66 (q, 4H, H$^{2,2'}$), 3.17 (t, 16H, H^c), 6.41 (dd, 2H, H$^{7,7'}$), 7.97 (dd, 2H, H$^{6,6'}$).

6. Yield: 1.53 g (88%). Anal. calcd (%) for **6** (C$_{48}$H$_{90}$N$_6$NiO$_4$, 873.96 g mol^{-1}): C 65.97, H 10.38, N 9.62; Found: C 65.22, H 10.50, N 9.79. IR: $\nu = 2961$(m), 2870(m) (CH); 1618(s), 1584(s), 1570(s) (CO). ^{1}H NMR: $\delta = 0.77$ (t, 6H, H$^{1,1'}$), 0.95 (t, 24H, H^a), 1.32 (m, 20H, H$^{2,2',b}$), 1.58 (m, 16H, H^c), 2.55 (m, 10H, H$^{3,3',DMSO}$), 3.17 (t, 16H, H^d), 6.41 (dd, 2H, H$^{8,8'}$), 7.97 (dd, 1H, H$^{7,7'}$).

Synthesis of [^{n}Bu$_4$N]$_2$[Cu(opboR$_2$)], R = Me (7), Et (8), ^{n}Pr (9).

A hot solution (*ca*. 50 °C) of [Cu$_2$(OAc)$_4$(H$_2$O)$_2$] (0.39 g, 0.001 mol) in MeOH (50 mL) was added dropwise with stirring to a hot suspension (*ca*. 50 °C) of **1**, **2** or **3** (0.002 mol), respectively, in MeOH (50 mL). Then, [^{n}Bu$_4$N]OH (5.18 g, 40% in MeOH, 0.008 mol) was added with continuous stirring. The resulting mixture was stirred at 60 ^{o}C for further 15 minutes, filtered and the solvent evaporated to dryness. The resulting oily material was treated with THF (25 mL) and filtered to eliminate [^{n}Bu$_4$N]OAc. The desired complexes were precipitated by addition of Et$_2$O (200 mL), as faint red powders, filtered and dried in *vacuo*. Crystals suitable for X-ray crystallographic studies were grown by slow diffusion of Et$_2$O into MeCN solutions of **7−9**. Figures S8−S10† give the IR spectra of **7−9**, respectively.

7. Yield: 1.26 g (78%). Anal. Calcd (%) for **7** (C$_{44}$H$_{82}$CuN$_6$O$_4$, 822.71 g mol^{-1}): C 64.24, H 10.05, N 10.22; Found: C 64.11, H 9.97, N 10.13. IR: $\nu = 2960$(m), 2881(m) (CH); 1616(s), 1587(s), 1568(s) (CO).

8. Yield: 1.44 g (85%). Anal. Calcd (%) for **8** (C$_{46}$H$_{86}$CuN$_6$O$_4$, 849.60 g mol^{-1}): C 65.94, H 10.19, N 9.88; Found: C 65.96, H 10.21, 9.68. IR: $\nu = 2964$(m), 2880(m) (CH); 1614(s), 1583(s), 1561(s) (CO).

9. Yield: 1.42 g (81%). Anal. Calcd (%) for **9** (C$_{48}$H$_{90}$CuN$_6$O$_4$, 877.63 g mol^{-1}): C 65.60, H 10.32, N 9.56; Found: C 65.21, H 10.05, N 9.29. IR: $\nu = 2963$(m), 2890(m) (CH); 1612(s), 1581(s), 1558(m) (CO).

Synthesis of [Cu$_3$(opboR$_2$)(pmdta)$_2$](NO$_3$)$_2$, R = Me (10), Et (11), ^{n}Pr (12).

To a solution of **7**, **8** or **9** (0.0006 mol) in MeCN (50 mL) was added a solution of [Cu(pmdta)(NO$_3$)$_2$] (0.43 g, 0.0012 mol) in MeCN (25 mL) dropwise with continuous stirring. After stirring for additional one hour, the resulting reaction mixture was

concentrated to approximately 5 mL and Et_2O (100 mL) was added to precipitate a green powder. The overlaying solvents mixture was removed *via* a Teflon tube and MeCN (5 mL) was added to dissolve the residue. A mixture of THF:Et_2O 4:1 (100 mL) was added to precipitate the product, which was washed twice with THF (100 mL). After removal of the supernatant, the remaining solid was dried in *vacuo*. Crystals suitable for X-ray crystallographic studies were grown by slow diffusion of Et_2O into a CH_2Cl_2 solution of **12**. **10**. Yield: 0.50 g (90%). Anal. Calcd (%) for **10** ($C_{30}H_{56}Cu_3N_{12}O_{10}$, 935.48 g mol^{-1}): C 38.52, H 6.03, N 17.97; Found: C 38.17, H 5.82, N 17.76. IR: ν = 2975(m), 2936(m), 2893(m) (CH); 1621(s), 1615(s) (CO); (1385)(s) (N=O). **11**. Yield: 0.48 g (84%). Anal. Calcd (%) for **11** ($C_{32}H_{60}Cu_3N_{12}O_{10}$, 963.53 g mol^{-1}): C 39.89, H 6.28, N 17.44; Found: C 39.59, H 6.06, N 17.12. IR: ν = 2970(m), 2927(m), 2890(m) (CH); 1616(s), 1609(s) (CO); (1381)(s) (N=O). **12**. Yield: 0.55 g (93%). Anal. Calcd (%) for **12** ($C_{34}H_{64}Cu_3N_{12}O_{10}$, 991.58 g mol^{-1}): C 41.18, H 6.51, N 16.95; Found: C 40.79, H 6.39, N 16.61. IR: ν = 2972(m), 2931(m), 2888(m) (CH); 1620(s), 1612(s) (CO); (1379)(s) (N=O). Figures S11−S13† give the IR spectra of **10**−**12**, respectively.

Crystals obtained from slow diffusion of Et_2O into CH_2Cl_2 solutions of **10** were of minor quality. Therefore, a metatheses reaction has been carried out. To a solution of **10** (0.0002 mol, 0.18 g) in MeOH (25 mL) was added a solution of $NaBPh_4$ (0.0005 mol, 0.17 g) in MeOH (25 mL) in one portion with stirring. A pale green powder was precipitate immediately, which was filtered off, washed thoroughly with MeOH and Et_2O and dried in *vacuo*. Slow diffusion of Et_2O vapour in a solution of the obtained powder in MeCN:DMF (1:1) mixture afforded single crystals of $[Cu_3(opboMe_2)(pmdta)_2](BPh_4)_2$ (**10'**) suitable for X-ray crystallographic studies after three days. No further characterization of **10'** has been carried out.

Remark for the crystallization of **11**: By allowing diffusion of Et_2O into MeCN solutions of **11** well shaped single crystals have been obtained. However, these crystals were too weakly diffractive and/or display very diffuse diffraction at higher diffraction angles, independent whether classical sealed-tube or µF Cu Kα radiation was applied. Due to this, a reliable refinement of the structure of **11** in the solid state was not possible.

Preparation of diamagnetically diluted single crystals (8@5 and 9@6).

To a solution of **5** or **6** (100 mg) in MeCN (5 mL) was added a solution of **8** or **9** (1 mg), respectively, in MeCN (1 mL) under stirring. After stirring for additional 24 hours in an open round bottom flask the volume of the mixture reduced to ca. 2.5 mL due to slow evaporation of the solvent. The remaining mixture was then transferred to a test tube and the diamagnetically diluted material allowed to crystallize under diffusion controlled conditions against Et_2O. Several orange coloured and non-hygroscopic single crystals with dimensions of ca. $0.4 \times 0.2 \times 0.2$ mm³ could be isolated after several days.

Any trials to grow sufficiently large single crystals of **7@4** failed, although for both of the individual complexes **4** and **7** comparatively large single crystals could be obtained. The obtained needle-like single crystals of the cocrystallization of **7** and **4** were of dimensions of ca. $0.1 \times 0.04 \times 0.04$ mm³ and were all orange coloured, which indicates that **7@4** was formed. Individual crystals were too small for an ESR characterization and a further characterization of them was not carried out.

X-ray crystallography

All data were collected on an Oxford Gemini S diffractometer. For data collection, cell refinement and data reduction the software CrysAlisPro was used.[28a] All structures were solved by direct methods using SHELXS-97 and refined by full-matrix least-squares procedures on F^2 using SHELXL-97 as part of the software package SHELXTL.[29a] All non-hydrogen atoms were refined anisotropically. All *C*-bonded hydrogen atoms were refined using a riding model.

Statements for the mononuclear complexes: In case of **4** a comparatively short distance between the hydrogen atoms of the corresponding carbon atoms C11 and C12 (methyl groups) is observed. The hydrogen atoms were here added on calculated positions as idealised methyl groups in staggered geometries (HFIX 33). The comparatively close vicinity of C11 and C12 is thus regarded as responsible for this artefact.

In case of **5'** and **8'** the positions of *O*-bonded hydrogen atoms were taken from the difference Fourier map and refined isotropically. Furthermore, for **5'** a comparatively large unrefined electron density peak is observed with ca. 0.7 e·Å^{-3} at a distance of ca.

1.8 Å away from O3. This peak might indicate a disorder of the respective water molecule, although this disorder could not be refined reliable.

The absolute structure of **6** was established by anomalous dispersion effects with respect to the absolute structure parameter.[30] Furthermore, the atoms C11, C13, C14 (0.84/0.16); the atoms C59, C60 (0.43/0.57); the atoms C69–C72 (0.34/0.66) and the atoms C73–C76 (0.72/0.28) are disordered and have been refined to split occupancies given in brackets. Although a number of atoms/groups could be refined disordered trials to refine more atoms/groups as disordered did fail or gave non-reliable results. This is most probably due to the comparatively low number of observed vs. total reflections. The two highest unrefined electron density peaks Q1 (ca. 1.6 e·$Å^{-3}$) and Q2 (ca. 1.2 e·$Å^{-3}$) are located ca. 1.1 Å away from Ni2 and ca. 1.1 Å away from Ni1, respectively.

In case of **9** the atoms C11, C13, C14 (0.47/0.53); the atoms C17–C20 (0.17/0.83); the atoms C21–C24 (0.32/0.68); the atoms C25–C28 (0.24/0.76); the atoms C33–C36 (0.65/0.35) and the atoms C37–C40 (0.37/0.63) are disordered and have been refined to split occupancies given in brackets. Several atoms her do have to large ADP max/min ratios or large Hirshfeld test differences and high U_{eq} values, respectively, when compared to neighbours. Furthermore, short intra and/or inter H··H contacts are observed. Most probably, all of these observations are due to further, but not reliable resolvable, disorder of atoms/groups. Additionally, the best suitable single crystal of **9** was, due to its plate-like shape, weakly diffractive only. Although long measurement times of individual frames have been applied by using Cu Kα radiation, the ratio between observed/unique reflections is with ca. 45 % still poor. Due to icing problems, the measurement has been stopped at a resolution of θ = ca. 60°. These reasons might explain why further models of disorder could not be introduced.

Data of **4**, **5'**, **6**, **7**, **8'** and **9** have been deposited at the Cambridge Crystallographic Data Centre under the CCDC deposition numbers CCDC 1035427-1035432, respectively.

Statements for the trinuclear complexes: In case of **10'** the trinuclear and dicationic complex fragment has been refined disordered on two positions. This disorder resembles a statistical disorder, whereby the complex fragments are arranged in top versus down orientation with respect to each other. The finally obtained and freely calculated occupation factors amounts to 0.68 versus 0.32. Several atoms appear as

further disordered as indicated by high U_{eq} values and large Hirshfeld Test differences when compared to neighbours. Trials to refine with SHELXL-2013 software[29b] by applying the RIGU command did not improve this situation. Their disorder could not be solved and refined reliable, which is mostly attributed to the already poor ratio of reflections to parameters.

In case of **12'** the crystals were twinned. By applying CrysAlisPro in version 1.171.37.31[28b] four different domains were applied for data integration. No further domains could be observed, whereby for domains I to IV the ratio 0.36, 0.32, 0.15 and 0.17, respectively, were finally determined. The SHELXL-2013 software[29b] was used for refinement and the command RIGU was applied. The two nitrate anions could be refined disordered over two positions (N11, O5–O7 (0.78/0.22) and N12, O8–O10 (0.34/0.66)). In addition, the atoms C11–C13 of one ^{n}Pr group could be refined disordered with occupations of 0.40/0.60. Furthermore, in the VOIDS one Et_2O and one CH_2Cl_2 molecule could be refined with occupation factors of 0.75 and 0.5, respectively. Thereby, the Et_2O molecule was refined disordered over two positions with occupation factors for O11, C36–C39 of 0.52/0.48.

Data of **10'** and **12'** have been deposited at the Cambridge Crystallographic Data Centre under the CCDC deposition numbers CCDC 10035433 and 1053078, respectively.

ESR measurements

The measurements of single crystals of **8@5** and **9@6** as well as liquid solution spectra of **8** and **9**, respectively, were recorded at room temperature on a Bruker EMX spectrometer operating in the X-band with a modulation frequency of 100 kHz. Handling of ESR spectra was carried out using Win-EPR® computer programs,[32a] spectral simulations were performed with Simfonia program.[33]

Electron Nuclear Double Resonance (ENDOR) experiments were performed with an X-band ESR spectrometer Elexsys E580 (Bruker) at a temperature of 20 K. A standard Davies ENDOR pulse sequence has been used: π_{mw}- π_{rf}- $\pi/2_{mw}$- π_{mw}-echo.[32b] In this pulse protocol the amplitude of the stimulated electron spin echo arising after the application of the microwave (mw) pulses π_{mw} - $\pi/2_{mw}$- π_{mw}-echo is recorded as a function of the frequency of the intervening radiofrequency (rf) pulse in the MHz range. To obtain the optimal rf π-pulse length (π_{rf}) the nutation experiments

were performed. For all measurements the lengths of the inversion pulse π_{mw}, radiofrequency pulse π_{rf} and detection pulses $\pi/2_{mw}$(π_{mw}) were set to 400 ns, 7 μs and 16 ns (32 ns), respectively. Simulations of the ENDOR spectra were performed using an EasySpin (version 4.0.0)[32c] program of the Matlab 2007a package.

Magnetic measurements

Static magnetic susceptibility was measured with a 7 T VSM-SQUID magnetometer from Quantum Design at a field of 1 T in a temperature range 2 – 300 K. In order to ensure the highest possible purity and to avoid any possible influence of partially liberated packing solvent from compounds due to storage, single crystals of **10**–**12** were evacuated for ca. 12 hours *in vacuo* and the complete loss of all solvent molecules has been ensured by an additional elemental analysis.

Quantum Chemical Studies

The density functional theory (DFT) calculations on individual, free molecules were carried out by using revision 2.80 of the ORCA code.[34] The Def2-TZVPP[35,36] basis set together with the B3LYP[37] functional was chosen to obtain a reasonable accuracy in our calculations and to have results comparable to previous investigations.[10] We used single molecules isolated from the measured X-ray data (were available) as input for our calculations. The counterions were neglected and further geometry optimizations were carried out using a gradient method. To check the optimization result the structures were compared to respective relaxed structures which were initially created from scratch using a molecular editor. We also compared the results to single point calculations using the unaltered crystallographic structures and did not find qualitative disagreements. The spin densities at the different atoms were calculated from the difference of the all electron density for minority (spin down) and majority (spin up) electrons followed by a numerical integration within spheres of radius R centred at the respective atoms. The same information was obtained by using Mulliken density analysis[38] as implemented in the ORCA code. In spite of giving slightly different numerical results for the respective absolute spin densities the results of both methods do agree very well and the same qualitative trends are observed.

Acknowledgments

References

1 E. Pardo, R. Ruiz-García, F. Lloret, M. Julve, J. Cano, J. Pasán, C. Ruiz-Pérez, Y. Filali, L.-M. Chamoreau and Y. Journaux , *Dalton Trans.*, 2008, 2780.

2 O. Kahn, *Molecular Magnetism*; VCH: New York, 1993.

3 R. Ruiz, C. Barland, A. Aukauloo, E. Mallart, Y. Journaux, J. Cano and M. Muñoz, *J. Chem. Soc., Dalton Trans.*, 1997, **5**, 745.

4 X. Ottenwaelder, A. Aukauloo, Y. Journaux, R. Carrasco, J. Cano, B. Cervera, I. Castro, S. Curreli, M. Munoz, A. Rosello, B. Soto and R. Ruiz, *Dalton Trans.*, 2005, 2516.

5 I. Fernandez, J. Pedro, A. Rosello, R. Ruiz, I. Castro, X. Ottenwaelder and Y. Journaux, *Eur. J. Org. Chem.*, 2001, 1235.

6 R. Ruiz, C. Surville-Barland, Y. Journaux, J.C. Colin, I. Castro, B. Cervera, M. Julve, F. LLoret and F. Sapina, *Chem. Mater.*, 1997, **9**, 201.

7 T. Sanada, T. Suzuki and S. Kaizaki, *J. Chem. Soc., Dalton Trans.*, 1998, 959.

8 a) M. A. Abdulmalic, A. Aliabadi, A. Petr, Y. Krupskaya, V. Kataev, B. Büchner, T. Hahn, J. Kortus and T. Rüffer, *Dalton Trans.*, 2012, **41**, 14657. b) The in ref. 8a reported experimentally determined J value of **14** has to be multiplied by 2 to comply with the spin Hamiltonia (6) of this report, yielding $J = -130$ cm^{-1}.

9 O. Kahn, *Angew. Chem., Int. Edn. Engl.*, 1985, **24**, 834.

10 B. Bräuer, F. Weigend, M. Fittipaldi, D. Gatteschi, E. J. Reijerse, A. Guerri, S. Ciattini, G. Salvan and T. Rüffer, *Inorg. Chem.*, 2008, **47**, 6633.

11 T. Rüffer, B. Bräuer, A. Powell, I. Hewitt and G. Salvan, *Inorg. Chim. Acta*, 2007, **360**, 3475.

12 T. Rüffer, B. Bräuer, F. Meva, B. Walfort, G. Salvan, A. Powell, I. Hewitt, L. Sorace and A. Caneschi, *Inorg. Chim. Acta*, 2007, **360**, 3777.

13 It should be emphasized that by applying the procedure reported for the synthesis of type **IV** complexes, related type **VI** complexes could not be obtained, at least

not in pure state. Thus, a new procedure was required for the synthesis of the desired type **VI** complexes **4**–**9**.

14 B. Cervera, J. L. Sanz, M. J. Ibanez, G. Vila, F. Lloret, M. Julve, R. Ruiz, X. Ottenwaelder, A. Aukauloo, S. Poussereau, Y. Journaux and M. C. Munoz, *J. Chem. Soc., Dalton Trans.*, 1998, 781.

15 J. E. Huheey, E. A. Keiter and R. L. Keiter, *Anorganische Chemie*, Walter de Gruyter, Berlin, New York, 2003, 2. Auflage, p. 134/135.

16 R. Costa, A. Garcia, J. Ribas, T. Mallah, Y. Journaux, J. Sletten, X. Solans, V. Rodriguez, *Inorg. Chem.*, **1993**, 32, 3733.

17 A. H. Maki and B. R. McGarvey, *Chem. Phys.*, 1958, **29**, 31.

18 J. R. Morton and K. F. Preston, *Magn. Reson.*, 1978, **30**, 577.

19 B. R. McGarvey, *J. Phys. Chem.*, 1967, **71**, 51.

20 Y. Krupskaya, A. Alfonsov, A. Parameswaran, V. Kataev, R. Klingeler, G. Steinfeld, N. Beyer, M. Gressenbuch, B. Kersting and B. Büchner, *Chem. Phys. Chem.*, 2010, **11**, 1961.

21 http://www.mpibac.mpg.de/bac/index_en.php/logins/bill/julX_en.php

22 V. Baron, B. Gillon, A. Cousson, C. Mathonière, O. Kahn, A. Grand, L. Öhrström, B. Delley, M. Bonnet and J.-X. Boucherle, *J. Am. Chem. Soc.*, 1997, **119**, 3500.

23 S. Pillet, M. Souhassou, C. Mathonière and C. Lecomte, *J. Am. Chem. Soc.*, 2004, **126**, 1219.

24 R. Costa, A. Garcia, R. Sanchez, J. Ribas, X. Solans and V. Rodriguez, *Polyhedron*, 1993, **12**, 2697.

25 D. D. Perrin and W. L. F. Armarego, *Purification of Laboratory Chemicals*, 3rd ed.; Pergamon: New York, 1988.

26 H. Stumpf, Y. Pei, O. Kahn, J. Sletten, and J. Renard, *J. Am. Chem. Soc.*, 1993, **115**, 6738.

27 G. Margraf, J. Bats, M. Wagner and H. Lerner, *Inorg. Chim. Acta*, 2005, **358**, 1193.

28 a) CrysAlisPro, Oxford Diffraction Ltd, Version 1.171.33.64 (release 22-03-2010 CrysAlis171.NET). b) CrysAlisPro, Agilent Technologies, Version 1.171.37.31 (release 14-01-2014 CrysAlis171 .NET).

29 a) G. M. Sheldrick, SHELXTL Version 5.1, *An Integrated System for Solving, Refining and Displaying Crystal Structures from Diffraction Data*, Siemens

Analytical X-ray Instruments, Madison, WI, 1990. b) G. M. Sheldrick, SHELXL2013, University of Göttingen, Germany (2013).

30 H. D. Flack, *Acta Crystallogr., Sect. A: Fundam. Crystallogr.*, 1983, **39**, 876.

31 A. Imre, A. Hellmann, G. Wenski, J. Graf, D. Johrendt and A. Mewis, *Z. Anorg. Allg. Chem.*, 2007, **633**, 2037.

32 a) R. T. Weber, J. J. Jiang and D. Barr, *EPR Division*, Software Version 2.3, Bruker Instruments, Inc, 1998. b) E. R. Davis, *Phys. Lett. A* 1974, **47**, 1. c) S. Stoll, A. Schweiger, *J. Magn. Reson.,* 2006, **178**, 42.

33 WinEPR Simfonia, Software Version 1.25**,** *a fast, easy to use EPR spectral simulation*, Bruker Analytical Instruments GmbH, 1996.

34 F. Neese, *Int. J. Quantum Chem.*, 2001, **83**, 104.

35 F. Weigend and R. Ahlrichs, *Phys. Chem. Chem. Phys.*, 2005, **7**, 3297.

36 A. Schaefer, H. Horn and R. Ahlrichs, *J. Chem. Phys.*, 1992, **97**, 2571.

37 A. D. Becke, *J. Chem. Phys.*, 1993, **98**, 5648.

38 R. S. Mulliken, *J. Chem. Phys.*, 1955, **23**, 1833.

Table 1 Selected bond lengths (Å) and angles (°) of **4A–9A** and of the [Cu(opboR$_2$)]$^{2-}$ fragments of **10A/10B** and **12A**

	4A[a]	5A[a,b]	6A/6B[a,c]	7A[d]	8A[b,d]	9A[d]	10A/10B[c,d]	12A[d]
				Bond lengths				
N1–M1	1.8485(16)	1.8546(15)	1.855(7) / 1.864(6)	1.938(16)	1.9374(17)	1.934(6)	1.953(9)/ 1.946(16)	1.953(11)
N2–M1	1.9033(16)	1.9130(16)	1.879(6) / 1.877(6)	1.952(17)	1.9645(18)	1.967(7)	1.985(7)/ 1.952(16)	1.986(13)
N3–M1	1.8508(15)	1.8546(15)	1.879(7) / 1.855(8)	1.938(17)	1.9374(17)	1.936(7)	1.926(9)/ 1.918(14)	1.933(11)
N4–M1	1.8989(16)	1.9130(16)	1.919(8) / 1.950(6)	1.953(17)	1.9645(18)	1.942(7)	1.991(7)/ 1.948(17)	1.992(12)
C1–O1	1.237(2)	1.247(2)	1.250(8) / 1.267(9)	1.239(2)	1.244(3)	1.244(3)	1.294(13)/ 1.28(4)	1.297(17)
C2–O2	1.247(2)	1.255(2)	1.275(8) / 1.274(8)	1.251(2)	1.258(3)	1.240(7)	1.297(13)/ 0.93(5)	1.278(19)
C3–O3	1.239(2)	1.247(2)	1.217(12)/ 1.243(11)	1.243(2)	1.244(3)	1.171(8)	1.43(3)/ 1.198(13)	1.262(16)
C4–O4	1.245(2)	1.255(2)	1.312(15)/ 1.263(9)	1.250(3)	1.258(3)	1.312(10)	1.296(14)/ 1.206(14)	1.300(17)
C1–C2	1.544(3)	1.539(3)	1.524(11)/ 1.493(12)	1.545(3)	1.551(3)	1.561(11)	1.527(17)/ 1.34(4)	1.47(2)
C3–C4	1.541(3)	1.539(3)	1.44(2) / 1.424(14)	1.548(3)	1.551(3)	1.559(14)	1.525(14)/ 1.396(13)	1.47(2)
				Bond angles				
N1–M1–N3	84.76(7)	84.26(9)	82.4(3) / 84.2(3)	82.20(7)	81.97(10)	80.8(3)	81.3(3)/ 80.6(6)	80.5(5)
N2–M1–N4	106.16(7)	108.24(10)	107.7(3)/ 104.8(3)	111.18(7)	112.38(11)	111.9(3)	110.3(3)/ 108.1(6)	112.9(5)
N1–M1–N2	84.66(7)	83.82(7)	83.6(3) / 85.8(3)	83.30(7)	83.03(7)	83.2(3)	83.9(3)/ 85.5(6)	83.6(5)
N3–M1–N4	84.47(7)	83.82(7)	86.3(4) / 85.2(3)	83.50(7)	83.03(7)	84.2(3)	84.5(3)/ 85.9(6)	83.4(5)
N1–M1–N4	169.09(7)	167.67(6)	168.7(3)/ 168.8(3)	165.23(7)	164.04(7)	164.9(3)	165.8(3)/ 166.3(6)	162.8(5)
N2–M1–N3	169.21(7)	167.67(6)	166.0(3)/ 169.9(3)	165.05(7)	164.04(7)	163.9(3)	165.1(3)/ 165.9(6)	163.2(5)
O1–C1–N1	128.27(19)	128.22(18)	126.4(7)/ 123.8(9)	128.7(2)	128.4(2)	128.2(10)	131.3(14)/ 120(3)	127.1(13)
O1–C1–C2	121.98(17)	121.40(18)	123.2(6)/ 122.5(7)	120.50(18)	120.22(19)	121.1(6)	115.3(11)/ 124(2)	119.0(13)
N1–C1–C2	109.75(16)	110.38(16)	110.3(6)/ 113.6(7)	110.79(18)	111.38(18)	110.7(7)	113.4(11)/ 116(3)	113.7(13)
O2–C2–N2	126.97(19)	128.00(19)	127.8(7)/ 129.1(8)	126.2(2)	127.2(2)	127.6(9)	126.6(11)/ 126(4)	124.2(15)
O2–C2–C1	119.29(18)	119.27(18)	119.0(6)/ 118.1(8)	118.68(19)	118.5(2)	117.4(7)	115.7(9)/ 114(3)	117.7(13)
N2–C2–C1	113.70(16)	112.72(17)	113.1(6)/ 112.7(6)	115.10(18)	114.31(18)	115.0(6)	117.6(11)/ 120(3)	118.1(15)
O3–C3–N3	128.47(18)	128.22(18)	127.1(14)/ 121.6(11)	128.3(2)	128.4(2)	132.8(13)	129.5(14)/ 127(2)	127.3(15)
O3–C3–C4	121.69(17)	121.40(18)	120.9(11)/ 127.2(9)	120.31(19)	120.22(19)	117.7(10)	118.2(9)/ 119.4(18)	119.8(12)
N3–C3–C4	109.84(16)	110.38(16)	111.8(9)/ 111.2(7)	111.42(18)	111.38(18)	109.4(7)	112.2(11)/ 113.7(17)	112.9(11)
O4–C4–N4	127.21(19)	128.00(19)	115.8(15)/ 121.1(9)	126.3(2)	127.2(2)	122.1(13)	127.1(11)/ 115.0(19)	124.5(13)
O4–C4–C3	119.43(17)	119.27(18)	126.4(11)/ 119.4(8)	119.0(2)	118.5(2)	122.0(8)	114.5(9)/ 126(2)	117.2(12)
N4–C4–C3	113.33(16)	112.72(17)	117.7(9)/ 118.8(7)	114.74(18)	114.31(18)	115.9(8)	118.4(10)/ 118.9(17)	118.1(12)

[a] M1 = Ni1. [b] For **5A/8A** the labeling is as follows: N3 = N1A, C3 = C3A, O3 = O1A, N4 = N2A, C4 = C4A, O4 = O4A. Symmetry code "A": –x, y, –z + ½. [c] The second entry belongs to analogous data of the crystallographically independent **B** molecule. [d] M1 = Cu1.

Table 2 Selected bond lengths (Å), angles (°) and $<\tau>$ parameters[16] of the terminal $[Cu(pmdta)]^{2+}$ fragments of **10A/10B** and **12A**.

	10A/10B	**12A**
	Bond lengths	
Cu2–O1	1.946(16)/1.97(3)	2.174(8)
Cu2–O2	2.030(10)/2.31(3)	1.982(9)
Cu2–N5	2.046(8)/2.06(3)	2.032(10)
Cu2–N6	2.031(8)/2.007(19)	2.004(10)
Cu2–N7	2.195(6)/2.076(10)	2.056(10)
Cu3–O3	2.043(12)/2.02(3)	2.179(8)
Cu3–O4	1.957(14)/2.15(4)	1.987(8)
Cu3–N8	1.992(9)/2.208(16)	2.058(10)
Cu3–N9	2.050(7)/2.05(2)	1.994(11)
Cu3–N10	2.209(8)/1.963(13)	2.077(11)
	Bond angles	
O1–Cu2–O2	83.3(4)/77.7(8)	81.3(3)
O1–Cu2–N5	140.6(7)/126.2(12)	107.8(4)
O1–Cu2–N6	99.6(4)/113.9(9)	103.1(4)
O1–Cu2–N7	97.9(6)/109.8(7)	98.9(4)
O2–Cu2–N5	88.0(4)/82.2(12)	92.8(4)
O2–Cu2–N6	173.7(4)/166.8(11)	175.6(4)
O2–Cu2–N7	98.4(3)/93.8(10)	93.2(4)
N5–Cu2–N6	86.2(4)/85.8(12)	85.8(4)
N5–Cu2–N7	121.5(3)/121.0(10)	153.2(4)
N6–Cu2–N7	86.8(3)/87.9(7)	86.2(4)
O3–Cu3–O4	86.5(7)/72.0(17)	80.7(3)
O3–Cu3–N8	127.8(7)/132.1(13)	106.8(4)
O3–Cu3–N9	99.4(7)/101.3(11)	102.5(4)
O3–Cu3–N10	105.7(6)/98.5(9)	98.7(4)
O4–Cu3–N8	89.8(4)/86.5(18)	92.3(4)
O4–Cu3–N9	173.9(5)/159.0(15)	176.8(4)
O4–Cu3–N10	92.4(5)/108.3(12)	93.0(4)
N8–Cu3–N9	88.1(4)/83.7(12)	86.7(4)
N8–Cu3–N10	126.5(4)/129.1(9)	154.4(4)
N9–Cu3–N10	84.2(3)/92.2(8)	86.6(4)
	$<\tau>$ parameter	
	0.644[a)]	0.373

a) The averaged $<\tau>$ parameter refers to the combination of **10A**/**10B**.

Table 3 Crystal and structural refinement data of **4**, **5'**, **6**, **7**, **8'** and **9**

	4	5'	6	7	8'	9
Chemical formula	$C_{44}H_{82}N_6NiO_4$	$C_{46}H_{90}N_6NiO_6$	$C_{48}H_{90}N_6NiO_4$	$C_{44}H_{82}CuN_6O_4$	$C_{46}H_{90}CuN_6O_6$	$C_{48}H_{90}CuN_6O_4$
Formula weight (g mol^{-1})	817.87	881.95	873.95	822.70	886.78	878.80
Crystal system	triclinic	monoclinic	monoclinic	triclinic	monoclinic	monoclinic
Space group	*P-1*	*C2/c*	*P2(1)*	*P-1*	*C2/c*	*P2(1)/c*
Unit cell dimensions (Å, °)	a = 10.7141(4)	24.3834(7)	13.5126(5)	10.583(13)	24.396(5)	13.4875(6)
	b = 14.4059(5)	13.4528(3)	14.7246(4)	14.534(3)	13.432(3)	14.6748(7)
	c = 15.4535(6)	15.9421(4)	25.4056(7)	15.609(15)	15.919(3)	25.6140(12)
	α = 99.540(3)	90	90	98.444(11)	90.0	90
	β = 90.910(3)	110.328(3)	95.567(3)	91.564(9)	109.80(3)	95.346(4)
	γ = 102.522(3)	90	90	102.014(12)	90.0	90
Volume (Å^3)	2292.92(15)	4903.7(2)	5031.0(3)	2318.8(5)	4908.4(19)	5047.6(4)
Measurement temperature (K)	110	110	110	100	100	100
Radiation source	Cu Kα	Mo Kα	Cu Kα	Cu Kα	Mo Kα	Cu Kα
Wavelengths (Å)	1.54184	0.71073	1.54184	1.54184	0.71073	1.54184
Z	2	4	4	2	4	4
Density (calculated) (Mg m^{-3})	1.185	1.195	1.154	1.178	1.200	1.156
Absorption coefficient (mm^{-1})	0.962	0.446	0.905	1.012	0.495	0.959
F(000)	896	1936	1920	898	1940	1924
Reflections collected	14594	10287	25119	17586	21633	14520
Independent reflections/$R_{int}$$^{a)}$	7226, 0.0212	4298, 0.0232	14709, 0.0265	6824, 0.0325	4293, 0.0225	7383, 0.0278
Index ranges	$-10 \le h \le 12$,	$-28 \le h \le 22$,	$-12 \le h \le 15$,	$-11 \le h \le 11$,	$-28 \le h \le 28$,	$-15 \le h \le 10$,
	$-16 \le k \le 16$,	$-15 \le k \le 15$,	$-16 \le k \le 16$,	$-16 \le k \le 16$,	$-15 \le k \le 15$,	$-16 \le k \le 16$,
	$-16 \le l \le 17$	$-18 \le l \le 16$	$-25 \le l \le 29$	$-17 \le l \le 17$	$-18 \le l \le 18$	$-28 \le l \le 25$
θ range for data collection (°)	3.19 to 61.99	2.96 to 25.00	3.47 to 61.98	3.91 to 60.63	2.96 to 25.00	3.29 to 59.99
Data / restraints / parameters	7226 / 0 / 496	4298 / 9 / 275	14709 / 479 / 1094	6824 / 0 / 496	4293 / 9 / 274	7383 / 804 / 715
Goodness-of-fit on $F^2$$^{b)}$	1.009	1.039	0.961	0.939	1.070	0.974
Final R indices [$I > 2\sigma(I)$]$^{c)}$	R_1 = 0.0423, wR_2 = 0.1171	R_1 = 0.0344, wR_2 = 0.0927	R_1 = 0.0991, wR_2 = 0.2531	R_1 = 0.0345, wR_2 = 0.0850	R_1 = 0.0368, wR_2 = 0.0933	R_1 = 0.0883, wR_2 = 0.2625
R indices (all data)$^{c)}$	R_1 = 0.0492, wR_2 = 0.1195	R_1 = 0.0452, wR_2 = 0.0950	R_1 = 0.1361, wR_2 = 0.2794	R_1 = 0.0497, wR_2 = 0.0892	R_1 = 0.0463, wR_2 = 0.1013	R_1 = 0.1498, wR_2 = 0.2980
Flack x parameter	–	–	0.10(5)	–	–	–
Largest diff. peak/hole (e·Å^{-3})	0.452, –0.398	0.710, –0.272	1.638, –0.301	0.226, –0.283	1.188, –0.376	0.320, –0.407

$^{a)}$ $R_{int} = \Sigma \left| F_o^2 - F_o^2(\text{mean}) \right| / \Sigma F_o^2$, where $F_o^2(\text{mean})$ is the average intensity of symmetry equivalent diffractions. $^{b)}$ $S = [\Sigma w(F_o^2 - F_c^2)^2]/(n - p)^{1/2}$, where n = number of reflections, p = number of parameters. $^{c)}$ $R = [\Sigma(||F_o| - |F_c|)/\Sigma|F_o|)$; $wR = [\Sigma(w(F_o^2 - F_c^2)^2)/\Sigma(wF_o^4)]^{1/2}$.

Table 4 Crystal and structural refinement data of **10'–12'**

	10'	12'
Chemical formula	$C_{78}H_{96}B_2Cu_3N_{10}O_4$	$C_{150}H_{290}Cl_4Cu_{12}N_{48}O_{43}$
Formula weight (g mol^{-1})	1449.89	4358.56
Crystal system	triclinic	monoclinic
Space group	*P-1*	*P2(1)/c*
Unit cell dimensions (Å, °)	$a = 13.7472(5)$	16.1788(11)
	$b = 14.0699(5)$	29.4708(15)
	$c = 19.3586(8)$	11.2788(7)
	$\alpha = 103.343(3)$	90.0
	$\beta = 100.238(3)$	91.797(7)
	$\gamma = 91.599(3)$	90.0
Volume (Å^3)	3576.0(2)	5375.1(6)
Measurement temperature (K)	100	100
Radiation source	Cu Kα	Cu Kα
Wavelengths (Å)	1.54184	1.54184
Z	2	2
Density (calculated) (Mg m^{-3})	1.347	1.346
Absorption coefficient (mm^{-1})	1.483	2.338
F(000)	1526	2286
Reflections collected	21468	21200
Independent reflections/R_{int}[a]	11034, 0.0370	11546, 0.1117
Index ranges	$-14 \leq h \leq 14$,	$-18 \leq h \leq 18$,
	$-16 \leq k \leq 16$,	$-33 \leq l \leq 34$,
	$-22 \leq l \leq 16$	$-13 \leq k \leq 13$
θ range for data collection (°)	3.24 to 62.00	4.059 to 63.50
Data / restraints / parameters	11034 / 434 / 1238	11546 / 716 / 691
Goodness-of-fit on F^2 [b]	1.039	0.939
Final *R* indices [$I > 2\sigma(I)$][c]	$R_1 = 0.0987$,	$R_1 = 0.0994$,
	$wR_2 = 0.2442$	$wR_2 = 0.2628$
R indices (all data)[c]	$R_1 = 0.1043$,	$R_1 = 0.1419$,
	$wR_2 = 0.2479$	$wR_2 = 0.2894$
Largest diff. peak/hole (e·Å^{-3})	0.713, − 0.656	1.564, −0.703

[a] $R_{int} = \Sigma \left| F_o^2 - F_o^2(\text{mean}) \right| / \Sigma F_o^2$, where $F_o^2(\text{mean})$ is the average intensity of symmetry equivalent diffractions. [b] $S = [\Sigma w(F_o^2 - F_c^2)^2]/(n - p)^{1/2}$, where n = number of reflections, p = number of parameters. [c] $R = [\Sigma(||F_o| - |F_c|)/\Sigma|F_o|)$; $wR = [\Sigma(w(F_o^2 - F_c^2)^2)/\Sigma(wF_o^4)]^{1/2}$.

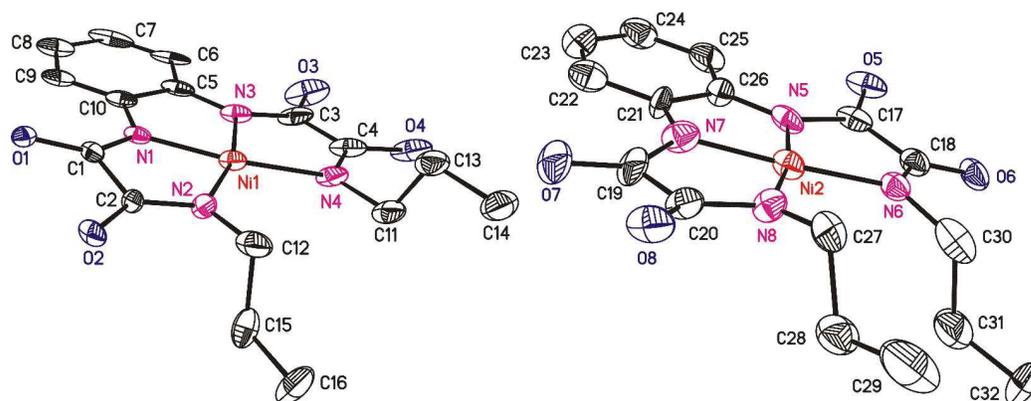## Supporting information

Figure S1 ORTEP diagram (25 % ellipsoid probability) of the molecular structures of **6A** (left) and **6B** (right). All hydrogen atoms are omitted for clarity.
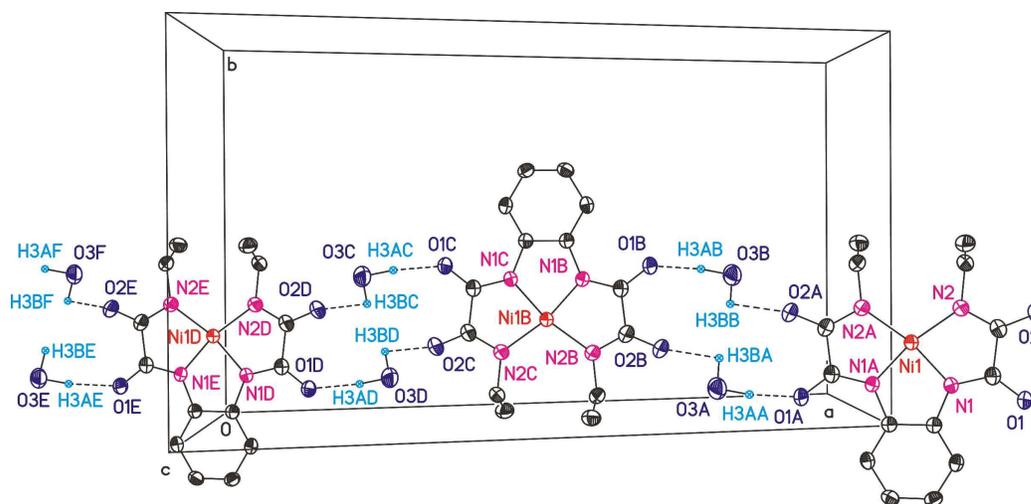

Figure S2 Graphical illustration of a selected part of one 1D chain formed by **5'** in the solid state due to formation of intermolecular hydrogen bonds. All [^{n}Bu$_4$N]$^+$ cations and *C*-bonded hydrogen atoms are omitted for clarity. Label "A" to "F" refers to atoms of a 1st to the 6th symmetry generated asymmetric unit of **5'**.

Table S1 Selected bond lengths (Å) and angles (°) of the intermolecular hydrogen bonds of **5'**.

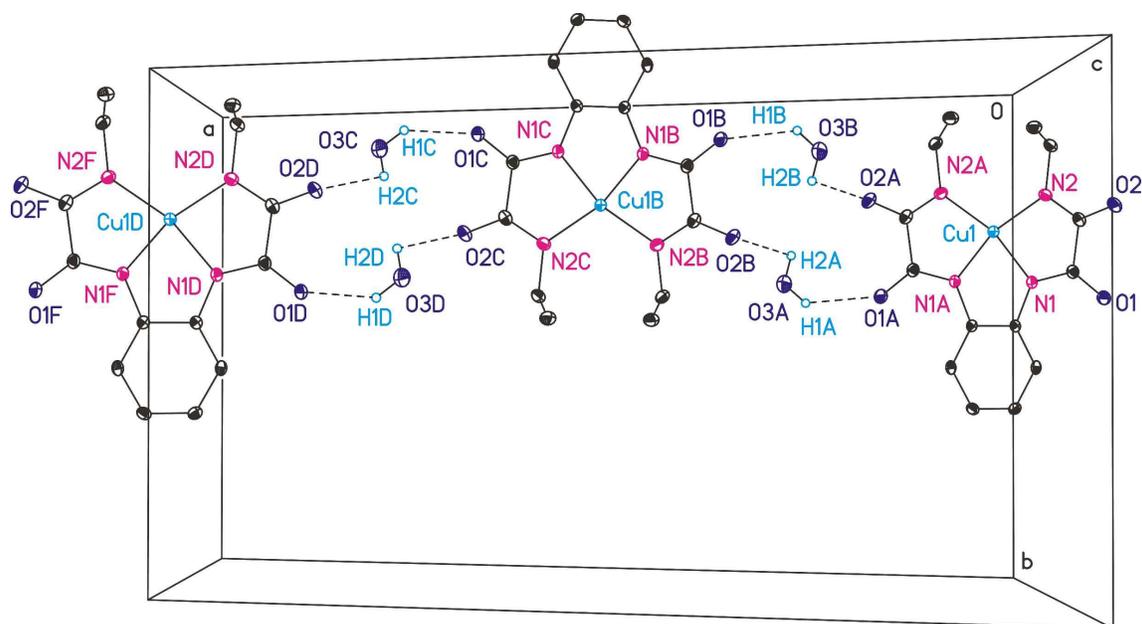| D–H···A	D···A	D–H···A
O3–H3A···O1	2.832(3)	124(3)
O3–H3B···O2^i	2.973(2)	111(3)

Symmetry code: (i) ½ − x, ½ − y, 1 − z.

Figure S3 Graphical illustration of a selected part of one 1D chain formed by **8'** in the solid state due to formation of intermolecular hydrogen bonds. All [$^nBu_4N$]$^+$ cations and *C*-bonded hydrogen atoms are omitted for clarity. Label "A" to "F" refers to atoms of a 1st to the 6th symmetry generated asymmetric unit of **8'**.

Table S2 Selected bond lengths (Å) and angles (°) of the intermolecular hydrogen bonds of **8'**.

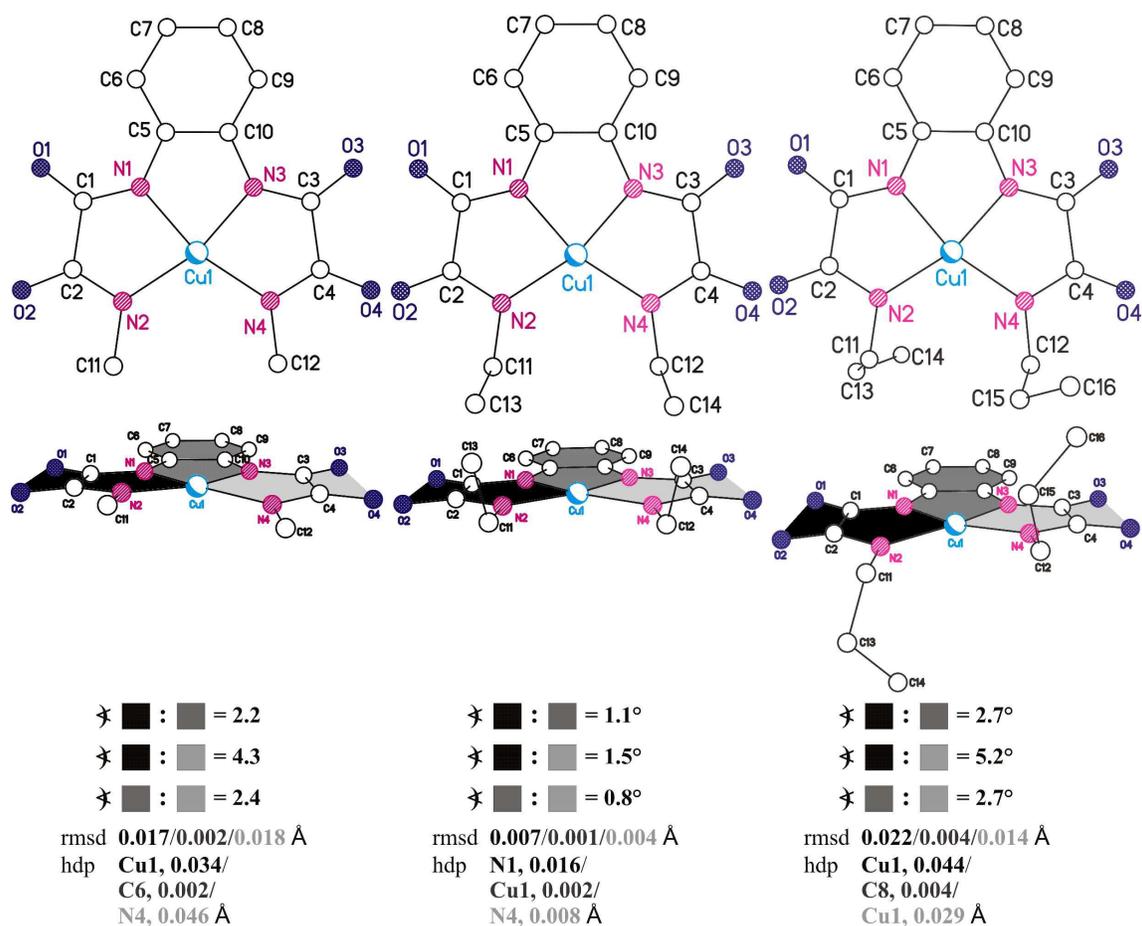| D–H⋯A	D⋯A	D–H⋯A
O3–H1⋯O1	2.830(3)	111(2)
O3–H2⋯O2^i	2.986(3)	115(2)

Symmetry codes: (i) ½ – x, ½ – y, 1 – z.

Figure S4 Ball-and-stick models of the molecular structures of **7A**^{calc}, **8A**^{calc} and **9A**^{calc} (left to right). Above: Top view. Below: Side view. All hydrogen atoms are omitted for clarity. The sign ✳ refers to the interplanar angles.

Table S3 Selected bond lengths (Å) and angles (°) of **7A–9A** and of the quantum chemically calculated related [Cu(opboR$_2$)]$^{2-}$ fragments denoted as **7A**^{calc}–**9A**^{calc}

	7A	7A^{calc}	8A^a	8A^{calc}	9A	9A^{calc}
			Bond lengths			
N1–Cu1	1.938(16)	1.970	1.9372(17)	1.974	1.934(6)	1.971
N2–Cu1	1.952(17)	2.001	1.9643(18)	2.011	1.967(7)	2.012
N3–Cu1	1.938(17)	1.971	1.9372(17)	1.973	1.936(7)	1.971
N4–Cu1	1.953(17)	2.001	1.9643(18)	2.009	1.942(7)	2.009
C1–O1	1.239(2)	1.235	1.244(3)	1.234	1.244(3)	1.234
C2–O2	1.251(2)	1.240	1.258(3)	1.240	1.240(7)	1.239
C3–O3	1.243(2)	1.235	1.244(3)	1.234	1.171(8)	1.234
C4–O4	1.250(3)	1.240	1.258(3)	1.240	1.312(10)	1.239
C1–C2	1.545(3)	1.564	1.551(3)	1.562	1.561(11)	1.563
C3–C4	1.548(3)	1.564	1.551(3)	1.563	1.559(14)	1.565
			Bond angles			
N1–Cu1–N3	82.20(7)	81.81	81.95(10)	81.65	80.8(3)	81.70
N2–Cu1–N4	111.18(7)	113.72	112.37(11)	113.96	111.9(3)	113.88
N1–Cu1–N2	83.30(7)	82.38	83.05(7)	82.18	83.2(3)	82.30
N3–Cu1–N4	83.50(7)	82.29	83.05(7)	82.22	84.2(3)	82.31
N1–Cu1–N4	165.23(7)	163.59	164.03(7)	163.83	164.9(3)	163.60
N2–Cu1–N3	165.05(7)	163.76	164.03(7)	163.82	163.9(3)	163.55
O1–C1–N1	128.7(2)	128.19	128.4(2)	128.20	128.2(10)	128.26
O1–C1–C2	120.50(18)	120.28	120.23(18)	120.21	121.1(6)	120.18
N1–C1–C2	110.79(18)	111.52	111.38(18)	111.60	110.7(7)	111.56
O2–C2–N2	126.2(2)	125.65	127.2(2)	125.91	127.6(9)	125.87
O2–C2–C1	118.68(19)	119.79	118.5(2)	119.41	117.4(7)	119.35
N2–C2–C1	115.10(18)	114.55	114.31(18)	114.68	115.0(6)	114.78
O3–C3–N3	128.3(2)	128.18	128.4(2)	128.22	132.8(13)	128.20
O3–C3–C4	120.31(19)	120.28	120.23(18)	120.18	117.7(10)	120.09
N3–C3–C4	111.42(18)	111.54	111.38(18)	111.59	109.4(7)	111.71
O4–C4–N4	126.3(2)	125.79	127.2(2)	125.94	122.1(13)	126.56
O4–C4–C3	119.0(2)	119.75	118.5(2)	119.43	122.0(8)	119.02
N4–C4–C3	114.74(18)	114.46	114.31(18)	114.63	115.9(8)	114.42

^{b} For **8A** the labeling is as follows: N3 = N1A, C3 = C3A, O3 = O1A, N4 = N2A, C4 = C4A, O4 = O4A. Symmetry code "A": –x, y, –z + ½.
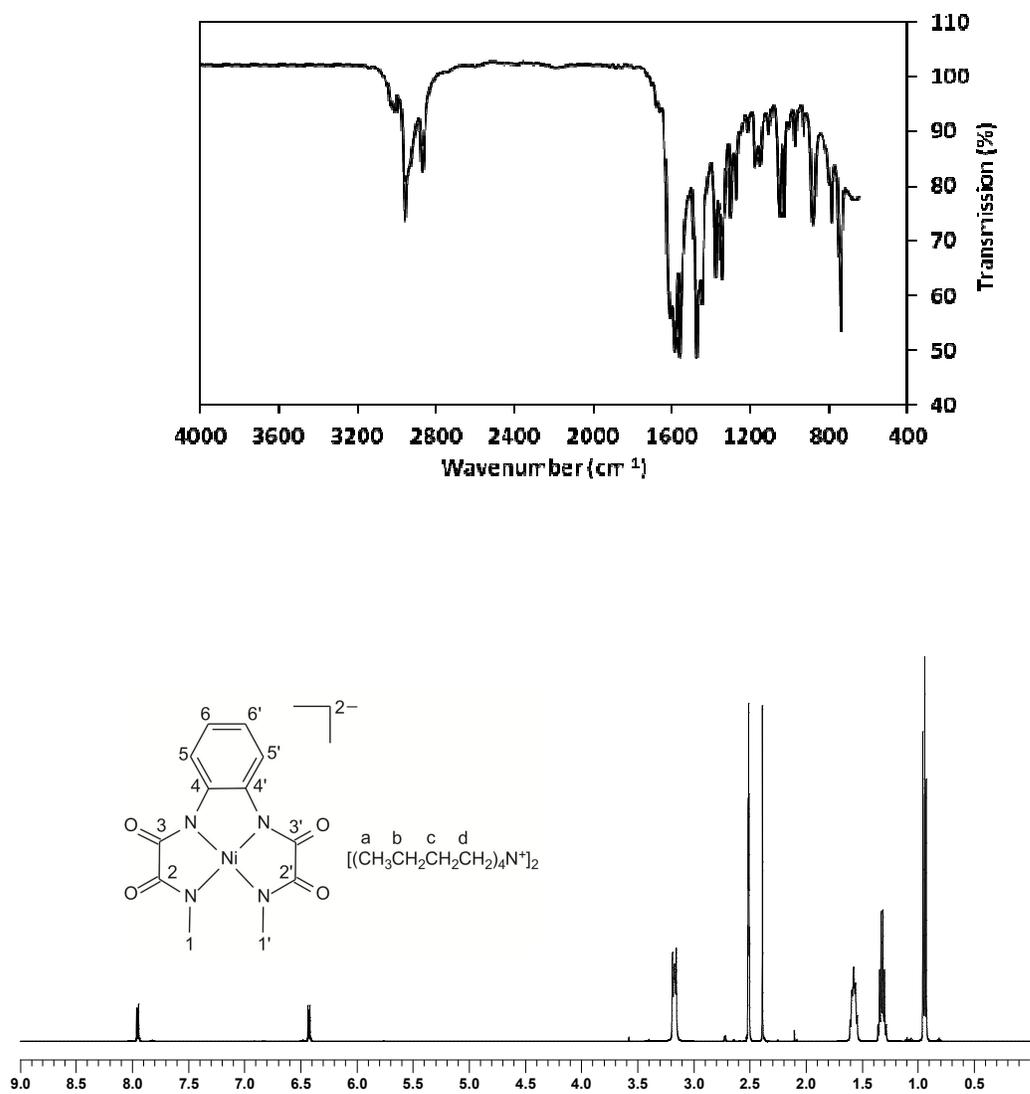
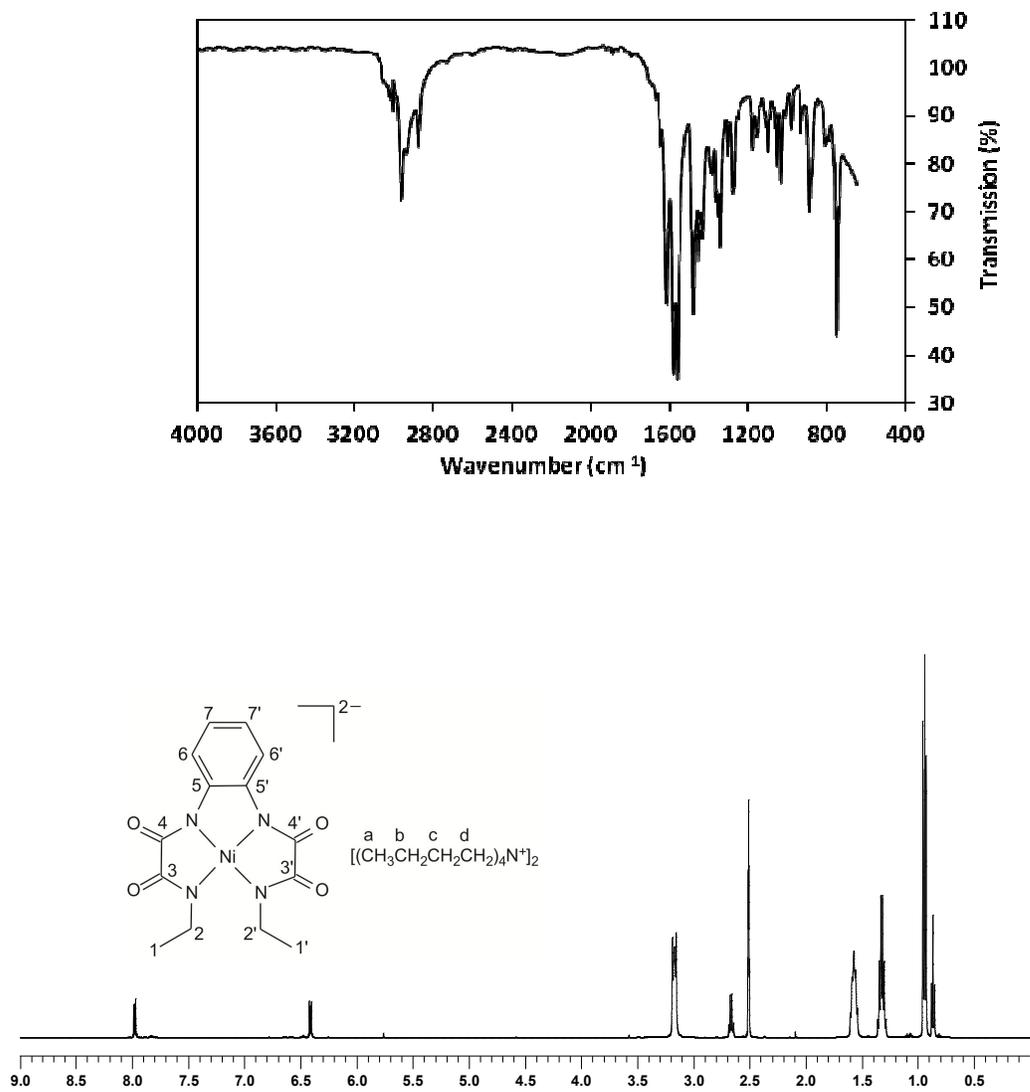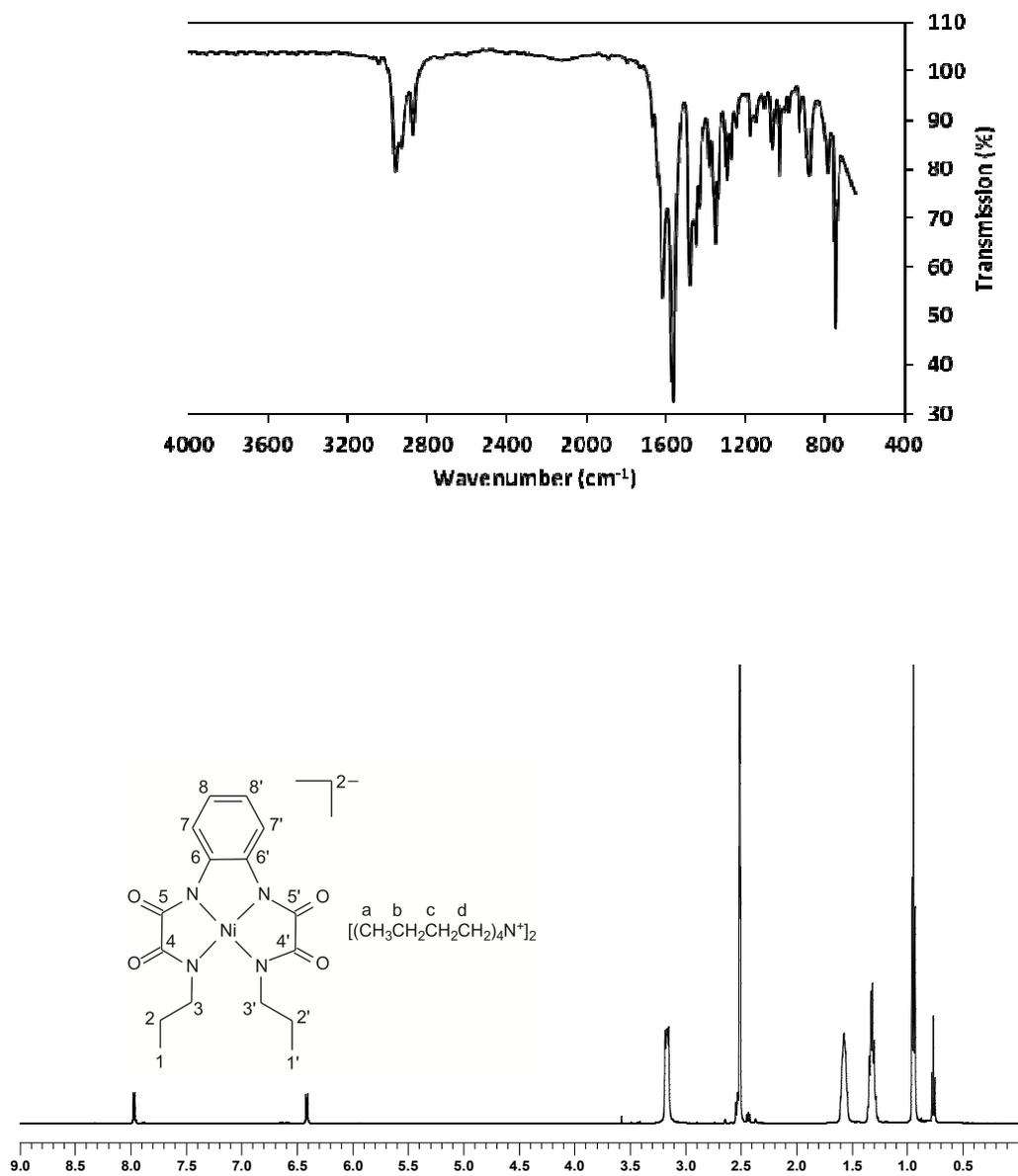**Figure S5** IR (above) and ^{1}H NMR (down) spectra of **4**

Figure S6 IR (above) and ^{1}H NMR (down) spectra of **5**

Figure S7 IR (above) and ^{1}H NMR (down) spectra of **6**
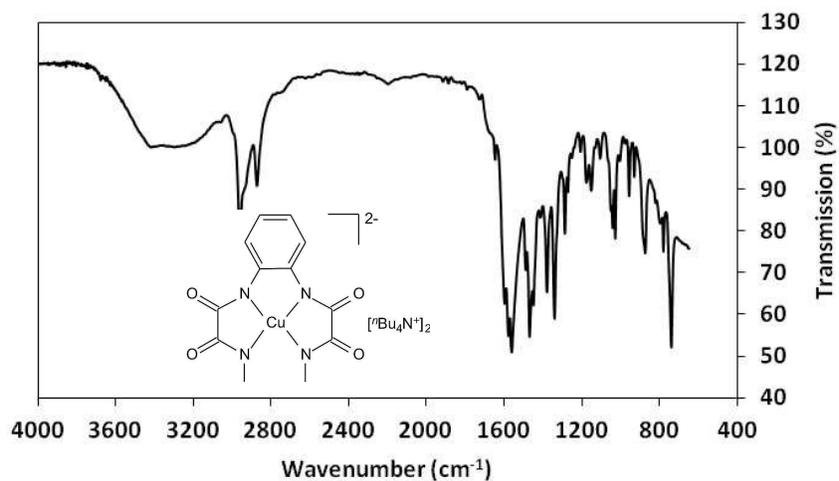
Figure S8 IR spectrum of **7**
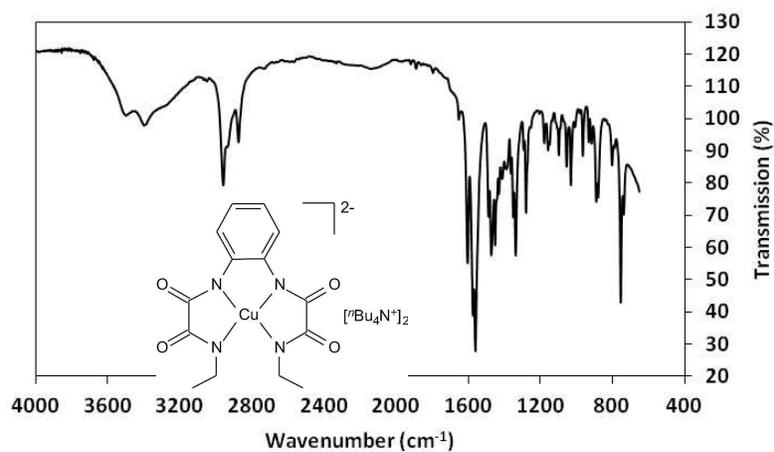
Figure S9 IR spectrum of **8**
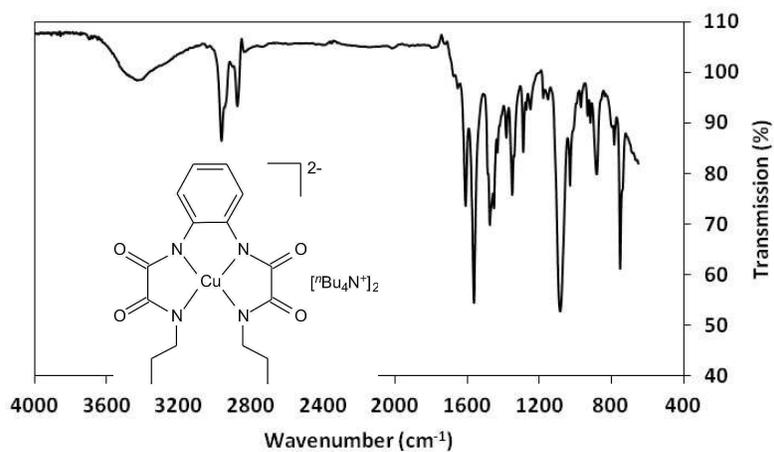
Figure S10 IR spectrum of **9**
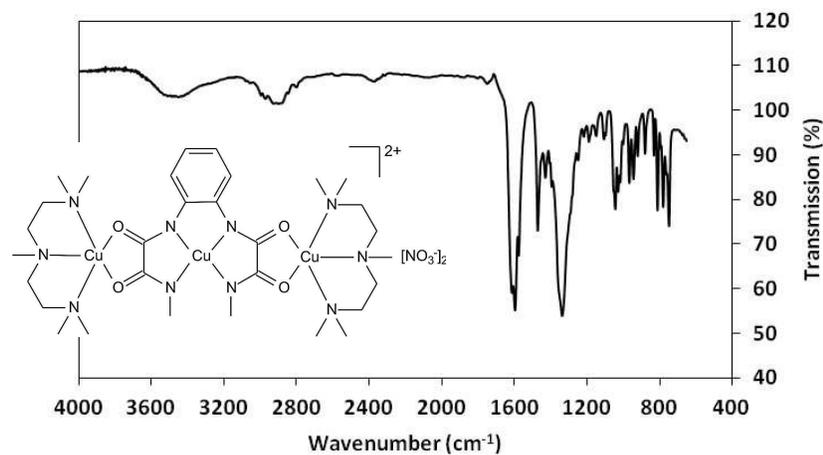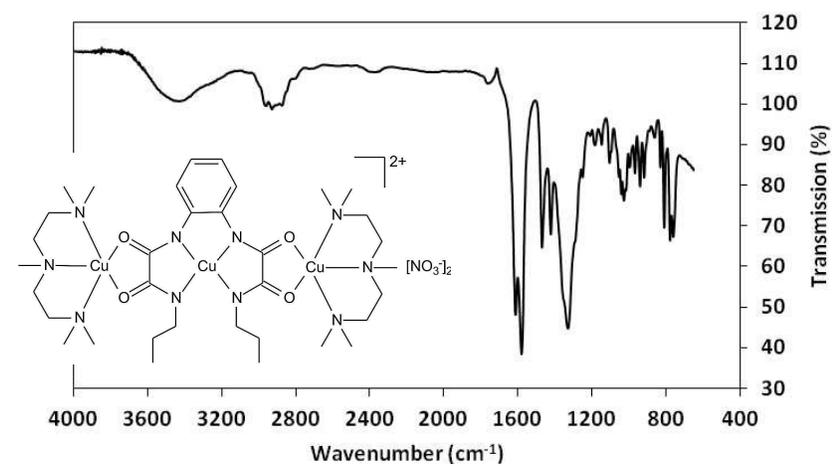
Figure S11 IR spectrum of **10**
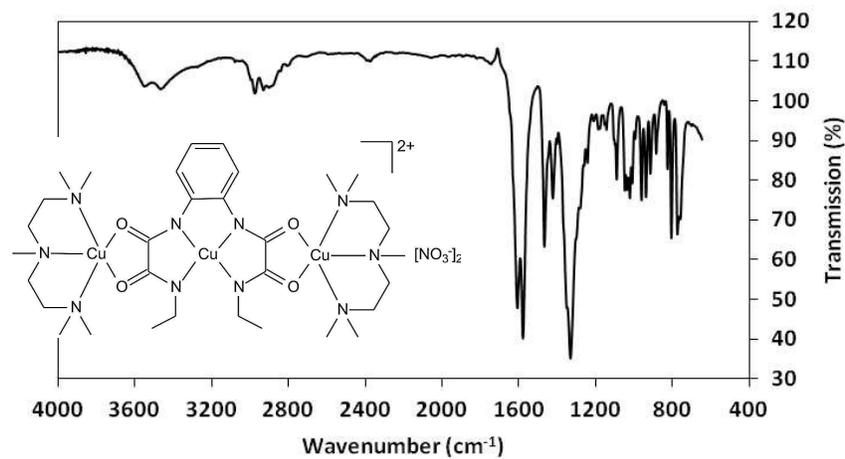
Figure S12 IR spectrum of **11**

Figure S13 IR spectrum of **12**